

## **Abstract**

JAEGER, DAVID. Electron Emission from Low Dimensional Structures. (Under the direction of Dr. John J. Hren).

A fundamental technological driving force is the search for simpler, more efficient and economical means of accomplishing a task. Nano-scale materials are seen as a means to efficiently emit electrons from a solid under the action of an electric field. The drive to smaller scales is also seen as a means to efficiently and simply produce devices. A thorough understanding of the characteristics of such materials is needed to understand and fully exploit these nano-materials when used as field enhanced electron emitters and efficiently process the devices.

The focus of this work was to investigate the effects that morphology, geometry and size can have on the electron emission characteristics of vacuum field emission cathodes. Deviations in surface structure and material strongly impact cathode reliability and performance due to the effect that these deviations have on the local surface electric field. Deterministically coating the cathode surface with material can positively impact cathode reliability and performance by manipulating surface morphology, band structure, thermal conductivity, and surface stability.

The local electrostatic field effects of nano-scale metallic and dielectric structures on metallic needles were investigated. The effects of needle arrays, dot size and position were analyzed for both metal and composite structures. Composite metal-insulator needles were investigated for effects of size and geometry of the insulator on electron emission. The field emission characteristics of a proposed electron source, designed for processing simplicity,

was analyzed. Effects of dimensionality and quantization of the surface electron gas on vacuum field emission was studied and a model of the emission process was developed.

Electrostatic shielding, triple junctions, multistage effects and geometric field enhancement were determined to be strongly affected by size, shape and morphology of the emitting structure. A condition for the saturation of the coherent tunneling current at high fields was found to be dependent on the band structure of the material. Coherent tunneling from low dimensional electron gases was found to be relatively insensitive to the dimensionality and quantization of the electron gas. Design criteria for a novel efficient microwave field emission cathode utilizing various low dimensional emission structures were also developed.

**ELECTRON EMISSION FROM LOW DIMENSIONAL STRUCTURES**

by  
**DAVID L. JAEGER**

A dissertation submitted to the Graduate Faculty of  
North Carolina State University  
in partial fulfillment of the  
requirements for the Degree of  
Doctor of Philosophy

**MATERIALS SCIENCE AND ENGINEERING**

Raleigh, NC

2006

**APPROVED BY:**

  
Gerald Iafrate

  
Olga Shenderova

  
John J. Hren  
Chair of Advisory Committee

  
Victor V. Zhirnov  
Co Chair of Advisory Committee

## **Biography**

David Jaeger was born in Kingston, NY on the 20<sup>th</sup> of January 1971. In 1982 he moved to Raleigh, NC with his family. He began his undergraduate studies at North Carolina State University in 1989 graduating with a Bachelor of Science in Physics. He later returned to North Carolina State University to pursue graduate studies under the direction of Professor John Hren, receiving a Masters degree in Materials Science and Engineering and remaining to pursue a Doctoral degree in Materials Science and Engineering.

## Acknowledgements

I would like to thank Dr. John Hren for the guidance, assistance and many discussions we have had and for agreeing to be my thesis adviser. Dr. Victor Zhirnov's passion and zeal for science and the unknown have been a constant inspiration to me and for this alone I wish to thank him. I thank Dr. Olga Shenderova and the International Technology Corporation for giving me the opportunity to work with them and broaden my horizons. I thank Dr. Gerald Iafrate for taking the time to serve as on my committee and agreeing to evaluate and aid in the development of my research.

I would also like to thank Dr. Dan Herr, Dr. Zhirnov and the Semiconductor Research Corporation for the opportunity to work with them on some novel and exciting concepts, much of which still inspires me. Finally I would like to thank the members of my research group, Talmage Tyler, Danielle Elswick and Greg Wojack, who have all provided invaluable advice, discussion and encouragement over the years.

## Table Of Contents

<b>List Of Figures.....</b>	<b>vii</b>
<b>List Of Tables .....</b>	<b>xii</b>
<b>Chapter 1. Introduction.....</b>	<b>1</b>
1.1. Motivation/Overview of Dissertation .....	1
1.2. Quantum Tunneling Formalism.....	2
1.3. Field Emission Formalism.....	5
1.4. Field Enhancement .....	7
1.5. Material effects .....	8
1.6. Thermal effects .....	9
1.7. Field Emission Applications.....	10
1.8. Fabrication of Field Emitters .....	10
1.9. Summary .....	11
1.10. References.....	12
<b>Chapter 2. Local electrostatic effects of surface structure on field emission: Metal on metal composite cathodes.....</b>	<b>18</b>
2.1. Abstract.....	19
2.2. Introduction.....	19
2.3. Simulation and Method.....	22
2.4. Results and Discussion .....	24
2.4.1. Idealized Single Tip Field Enhancement Effects.....	24
2.4.2. Multistage Field Enhancement Effects .....	27
2.4.3. Geometrically Inhomogeneous Needle Field Enhancement Effects.....	31

2.5. Conclusions.....	32
2.6. References.....	33
<b>Chapter 3. Electrostatic effects of conformal and isolated diamond nanodots on field emission.....</b>	<b>48</b>
3.1. Abstract.....	49
3.2. Introduction.....	49
3.3. Experimental Input .....	51
3.4. Numerical Method.....	52
3.5. Results and Discussion .....	52
3.6. Conclusions.....	55
3.7. Acknowledgements.....	56
3.8. References.....	56
<b>Chapter 4. Field Emission Device with Back-Gated Structure .....</b>	<b>64</b>
4.1. Abstract.....	65
4.2. Introduction.....	65
4.3. Experiments .....	68
4.3.1. Fabrication of the back-gated device structure .....	68
4.3.2. Cathode-Gate Model: Cylinder-Plane geometry.....	69
4.3.3. Simulation Setup.....	71
4.4. Results and Discussion .....	74
4.5. Conclusions.....	76
4.6. Acknowledgements.....	77
4.7. References.....	78
<b>Chapter 5. Cold Field Electron Emission from 0D, 1D And 2D Electron Gases .....</b>	<b>87</b>
5.1. Abstract.....	88

5.2. Introduction.....	88
5.3. Tunneling Equations .....	89
5.4. Results and Discussion .....	95
5.5. Conclusions.....	99
5.6. References.....	99
<b>Chapter 6. Summary .....</b>	<b>110</b>
6.1. Geometric electrostatic field effects on field emission.....	110
6.2. Dimensionality effects on field emission.....	111
6.3. Suggested Future Work .....	111
6.4. References.....	112

## List Of Figures

### 1 Introduction

- 1 Conventional Fowler Nordheim emission from the partially filled conduction band of a metal cathode source into a collector through a triangular barrier potential. Current from the collector to the source is considered negligible. Electron emission is peaked near the Fermi level as shown in the schematic TED. .... 16
- 2 Temperature along the axis of an emitter for times 1,2,3,4; where  $t_1 < t_2 < t_3 < t_4$ . .... 17

### 2 Local electrostatic effects of surface structure on field emission: Metal on metal composite cathodes

- 1 Planar diode geometry with ellipsoidal needle, appropriate boundary conditions approximating the experimental domain modeled and geometrical parameters. .... 38
- 2 HRTEM profile of an electrochemically etched Mo needle exhibiting a nonhomogeneous profile with many surface features. .... 39
- 3 Field enhancement factors versus aspect ratio for ellipsoidal emitters using numeric and analytical methods. (a) exact analytic expression of Eq. (3c), (b) a common experimental approximation,  $\gamma \approx h/r + 2$ , and (diamonds) the FiEM result. .... 40
- 4 Potential normal to the ellipsoidal needle apex calculated using several methods. (solid line) the FiEM numeric approach, (diamonds) the exact analytic formula Eq. (3a), (crosses) an approximate form of the potential given by Eq. (4a), and (circles) the modified formula of Eq. (4a) given by Eq. (4b). .... 41
- 5 Field enhancement across the emitter surface for a two stage composite needle. (squares) a base needle with  $r_c = 200\text{nm}$ , (diamonds) a protrusion with  $r_c = 3\text{nm}$  on the surface of the base needle, and (circles) a protrusion with  $r_c = 0.625\text{nm}$  on the surface of the base needle. .... 42
- 6 Percent error between the MSFE model and numerical results using the Finite Element Method for various types of idealized inhomogeneities on elliptic and spherical needle substrates. (a) spherical particle embedded on spherical substrate, (b) ellipsoidal particle embedded on spherical substrate, (c) spherical particle embedded on ellipsoidal substrate, (d) ellipsoidal particle embedded on ellipsoidal substrate. .... 43
- 7 Field magnification values as a function of the number of substructures consisting of embedded spheres of decreasing radii. (a) FiEM numeric results, (b) results of the ideal MSFE model using Eq. (6). .... 44

8	Potential profile of a composite metal needle using FiEM numeric results. Applied anode voltages of (a) 0V, (b) 100V, (c) 200V, (d) 300V, (e) 400V, (f) 500V, (g) 600V, and (h) 700V. ....	45
9	HRTEM image of the simulated needle. ....	46
10	The geometric approximation of Figure 9 and the resultant field distribution.....	47
<b>3 Electrostatic effects of conformal and isolated diamond nanodots on field emission</b>		
	Figure 1. Field distribution near the apex of a metal insulator composite needle exhibits behavior strongly dissimilar to that experienced by a wholly metal composite needle; particle radius is 5nm $\epsilon_r = 5.7$ and an applied bias of 1000V... ..	58
	Figure 2. Extracted field enhancement values along the metal-diamond (MD), metal-vacuum (MV), diamond-vacuum (DV) and metal-diamond-vacuum (MDV) interface surfaces for the embedded nanodiamond particle model system with particle radii of $r=5\text{nm}$ and relative permittivity of $\epsilon_r = 5.7$ .....	59
	Figure 3. Electrostatic field enhancement at several points of interest, dm – metal diamond interface, dv – diamond vacuum interface and dmv – metal diamond vacuum interface, as a result of varying the dielectric permittivity of the particle for a) conformal particle and b) semi-embedded particle of radius 5nm. ....	60
	Figure 4. Electrostatic field enhancement at several points of interest, dm – metal diamond interface, dv – diamond vacuum interface and dmv – metal diamond vacuum interface, as a result of varying the particle radius for a) conformal particle and b) semi-embedded particle of relative dielectric permittivity 5.7.....	61
	Figure 5. Electrostatic conduction band potential normal to the center of revolution of a composite needle for a) a conformal particle and b) a semi-embedded particle of radius 5nm and an applied bias of 1000V.....	62
	Figure 6. Electrostatic conduction band potential normal to the center of revolution of a composite needle as a function of particle radius for a) conformal particle and b) semi-embedded particle of relative dielectric permittivity 5.7 and an applied bias of 1000V. ....	63
<b>4 Field Emission Device with Back-Gated Structure</b>		
1	Schematic representation of the back gated device with cathodes implemented as wire arrays (left). Enlarged view of the cathode (right), containing field emitting material (low work function material or carbon nanotube/polymer composite, for example) at the top. Other EMS alternatives could be used, such as tips fabricated at the top of the cathode. ....	80

- 2 Field above the cathode for cylindrical cathode (a) and a cathode rectangular in its cross section (b). Cathodes profiles are shown in the left up corners. Field is shown as a function of the angular coordinate (a) and as a function of length along the rectangle perimeter (b). Anode voltage is 500V, cathode-anode distance is 1 mm, cathode-gate distance is 3  $\mu\text{m}$ , dielectric constant of the insulator layer equals 4. Diameter of a cylindrical cathode is 2  $\mu\text{m}$  (a), sizes of rectangles in a cross section of cathode (b) are 2x2 $\mu\text{m}^2$  ( $\diamond$ ) and 2x4  $\mu\text{m}^2$  ( $\blacksquare$ ). Dashed horizontal lines in (a) correspond to typical macroscopic fields required to initiate field emission from material containing carbon nanotube ( $E_{CNT}$ ) and from metallic flat surface ( $E_{Me}$ ). ..... 81
- 3 Schematic general model of the back gate structure and SWCNT arrays on a cathode substrate wire with relevant material and boundary condition parameters indicated. (acronyms BGD and EMS stand for back gate dielectric and emissive material/structure, respectively). ..... 82
- 4 Variation of the emission and electrostatic properties for the optimized SWCNT EMS structure, a) integrated current  $I_{Device}$  and maximum electrostatic field at the EMS surface  $E_{SWCNT}$ , b) capacitance of the back gate structure C, as a function of the separation between the gate metal cathode lines  $w_{wire}$ . Relevant parameters used:  $\Phi_{Gate} = 30V$ ,  $\Phi_{Anode} = 200V$ ,  $h_{BGD} = 3.1\mu\text{m}$ ,  $h_{gap} = 20\mu\text{m}$ ,  $\gamma_{SWCNT} = 500$ ,  $\epsilon_{BGD} = 4$ . ..... 83
- 5 Variation of the maximum integrated current  $I_{optimized}$  and gate metal cathode line separation  $w_{max}$  with the gate bias  $\Phi_{gate}$ . Relevant parameters used:  $\Phi_{Anode} = 200V$ ,  $h_{BGD} = 3.1\mu\text{m}$ ,  $h_{gap} = 20\mu\text{m}$ ,  $\gamma_{SWCNT} = 500$ ,  $\epsilon_{BGD} = 4$ . ..... 84
- 6 Variation of the integrated current  $I_{Device}$  and maximum electrostatic field at the EMS surface  $E_{SWCNT}$  with the back gate dielectric structure and material parameters; a) dielectric permittivity  $\epsilon_{BGD}$ , b) thickness  $h_{BGD}$ . Relevant parameters used:  $\Phi_{gate} = 30V$ ,  $\Phi_{Anode} = 200V$ , a)  $h_{BGD} = 3.1\mu\text{m}$ ,  $h_{gap} = 20\mu\text{m}$ ,  $\gamma_{SWCNT} = 500$ , b)  $\epsilon_{BGD} = 4$ ,  $w_{wire} = 6.4\mu\text{m}$ . ..... 85
- 7 Variation of the integrated current  $I_{Device}$  and transconductance  $g_{gate}$  with the cathode substrate shape and the gate bias  $\Phi_{gate}$ ; a) a  $\frac{1}{2}$  cylinder of  $r_{wire} = 0.47\mu\text{m}$ , b) a trapezoidal line of  $2r_{wire} = 0.94\mu\text{m}$  and  $h_{wire} = 0.3\mu\text{m}$ . Relevant parameters used:  $\Phi_{Anode} = 200V$ ,  $h_{BGD} = 3.1\mu\text{m}$ ,  $h_{gap} = 20\mu\text{m}$ ,  $\gamma_{SWCNT} = 500$ ,  $\epsilon_{BGD} = 4$ ,  $w_{wire} = 6.4\mu\text{m}$ . ..... 86

## 5 Cold Field Electron Emission from 0D, 1D And 2D Electron Gases

Figure 1. Schematic of general low dimensional electron emitting structures, in blue, and the surrounding bulk material that constitute the active region of a field emitter cathode. Electron emission occurs in the z axis direction and the relative length of the axis vectors indicates the degree of electron confinement in those particular directions. The tunneling electron is emitted from a surface

electron gas whose dimensionality varies horizontally and degree of quantization varies vertically..... 102

Figure 2. General triangular potential seen from an electron traversing from the left at energy  $E_z$ , where  $E_b$  is the band minimum,  $E_f$  is the Fermi energy,  $E_p$  is ideally the energy at which a maximum amount of electrons can quantum mechanically tunnel through the potential barrier, and  $E_T$  is the top of the potential barrier, typically the local vacuum level. .... 103

Figure 3. Analytical FN and numerical QTBM calculations of (a) current densities and (b) Linearized Fowler-Nordheim plots, denoted by lines and markers respectively, for the case of d-dimensional structures with continuous bands and parameters  $E_b = -10.6eV$ ,  $E_f = -4.6eV$ , and  $E_p = E_f$ , displaying classical Fowler-Nordheim tunneling where electron emission is limited by quantum barrier tunneling. .... 104

Figure 4. Analytical FN and numerical QTBM calculations of (a) current densities and (b) Linearized Fowler-Nordheim plots, denoted by lines and markers respectively, for the case of d-dimensional structures with continuous bands and parameters  $E_b = -0.8eV$ ,  $E_f = -0.4eV$ , and  $E_p = E_f$ , displaying saturation behavior where electron emission is limited by quantum barrier tunneling in region I and by the electron supply in region II. .... 105

Figure 5. Analytical FN calculations of transconductance for the case of low dimensional structures with continuous bands and parameters  $E_b = -0.6eV$ ,  $E_f = -0.4eV$ , and  $E_p = E_f$ , where the approximate onset of saturation behavior is observed near the maximum transconductance. .... 106

Figure 6. From WKB numerical current densities the calculated FN parameters  $E_p$  and  $\gamma_{FN}$ , denoted by lines and lines + markers respectively, are shown for low dimensional structures with continuous bands and parameters  $E_f = -0.4eV$ ,  $E_p = E_f$  and  $\gamma_{FN} = 20$ . The applied fields were limited up to the maximum transconductance. .... 107

Figure 7. The percent of electrons emitted and the saturation transconductance ratio,  $g(F_{max})/g_{max}(F)$ , at the maximum transconductance, denoted by lines and lines + markers respectively, for low dimensional structures with continuous bands and parameters  $E_f = -0.4eV$  and  $E_p = E_f$ . The threshold energies at which the saturation component has an effect on the emission process are indicated by  $E_{t,nD}$  at the top of the graph. .... 108

Figure 8. From WKB numerical calculations the variation of the saturation threshold energies,  $E_t$ , and the energy at which the saturation FN equations agree within 80% to the pure FN equations,  $E_s(0.8)$ , denoted by lines and markers respectively, are shown for low dimensional structures with continuous bands and parameters  $E_p = E_f$  and  $\gamma_{FN} = 20$  ..... 109

## List Of Tables

### 1 Introduction

I	General Properties of Solid-State and Field Emission Devices .....	14
II	Processes used for fabrication of specific emitter structures, including the approximate number of masks, total fabrication steps and amount of energy and material required.....	15

### 2 Local electrostatic effects of surface structure on field emission: Metal on metal composite cathodes

I	Degree of agreement between analytical and numerical approaches for various model geometries.....	36
II	Percent error between analytic models and numerical results for the maximum field enhancement achievable at the composite needle surface. ....	37

### 4 Field Emission Device with Back-Gated Structure

I	Physical parameters used in the Fowler-Nordheim current analysis.....	79
---	---	----

### 5 Cold Field Electron Emission from 0D, 1D And 2D Electron Gases

I	Fit parameters for the least squares analysis of the general FN plot analysis and extracted material parameters.....	101
---	--	-----

## Chapter 1. Introduction

### 1.1. Motivation/Overview of Dissertation

The primary goal of the work contained within this dissertation is to examine how the field emission process is affected by variations in geometry and material for reduced scale materials. This work was motivated by the need to optimize the performance of vacuum microelectronic devices that incorporate low-dimensional structures, which allow possible performance and fabrication benefits. Previous research involving coatings of wide band gap materials, deposited using plasma and chemical vapor deposition (CVD) techniques, on Si arrays at North Carolina State University (NCSU)<sup>1</sup>, Moscow Institute of Crystallography (IOC)<sup>2</sup> and MCNC (Durham, NC)<sup>3</sup> indicated that coatings could be used to improve field emission properties. It was also found that coating by electrophoresis was a relatively energy efficient method, compared to plasma and CVD techniques, for depositing diamond nanoparticles. These nanoparticle coatings also demonstrated improved field emission properties and as field emitters the ability to investigate the properties of discrete nanoscale structures. Research on a vacuum microelectronic device designed for microwave tube applications at the International Technology Center – ITC (Durham, NC)<sup>4</sup> indicated that the device could be efficiently fabricated relative to conventional designs.

The general emission characteristics and the factors influencing those characteristics of conventional metal and semiconductor field emitter structures, such as etched needles, gated and un-gated arrays, is well understood, while those for thin film and particulate coatings is not as well understood<sup>5</sup>. However many of these methods require growth of the emitting structures which is relatively costly and time consuming. Deposition of the

emitting structures by means of techniques such as slurries<sup>6</sup> and electrophoresis<sup>7</sup> have been used to reduce the cost and time required to fabricate a device, while retaining the benefits of the material. The properties of the deposited coatings typically are not as well controllable as the grown coatings, such that the morphology, orientation, size and dimensionality of the coating can affect the cathodes emission characteristics<sup>5</sup>. Therefore many more parameters affect emission for devices incorporating these coatings, making the optimization, characterization and analysis of these structures extremely difficult. The analysis of the effect that several of these parameters have on the emission characteristics of field emission cathodes consisting of low-dimensional structures on micron sized needles therefore was the primary objective of this work.

## 1.2. Quantum Tunneling Formalism

The calculation of the tunneling current through some interface fundamentally requires a model Hamiltonian, the barrier Hamiltonian, describing the region. The tunneling Hamiltonian originates from the molecular Hamiltonian that describes condensed matter as an interacting many electron and ion system with externally applied fields.

The time dependent Schrödinger equation provides all information related to the tunneling process. Assuming we can decouple the electronic and nuclear components of the molecular Hamiltonian we can describe the molecular wave function as the product of the electronic wave function and the nuclear wave function. Assuming that the electrons can instantaneously react to changes in the nuclei configuration, the adiabatic approximation is applied to the nuclear component of the Schrödinger equation. If the energy variation of the electronic Hamiltonian is small over the time  $h/\Delta E_n$  compared to  $\Delta E_n$ , for a 10eV barrier

this results in a frequency of  $\sim 1000\text{THz}$ , then the adiabatic approximation is valid with regards to the electronic Schrödinger equation, resulting in the time independent Schrödinger equation. The time independent approach is the typical method used in most Field Emission analysis, however in the case of field emitters interacting with a microwave field operating at very high frequencies,  $>100\text{THz}$ , this conventional analysis will fail since the Field Emission process is no longer adiabatic<sup>8</sup>.

Two general methods have been developed to solve the electronic Schrödinger equation, electronic structure and phenomenological band structure methods. Electronic structure methods, such as density functional theories, typically are restricted to small systems and numerical analysis, but they provide accurate information on surface electronic structure. Band structure methods, such as the one-electron effective mass method, parameterize the potential barrier component of the barrier Hamiltonian such that infinitely large systems are assumed and electronic structure is approximated. Field emission studies typically use the one-electron effective mass method since atomic scale resolution of charge distributions is not typically required<sup>9</sup>.

Taking the view that tunneling at interfaces is a one electron and effectively stationary process the dynamics of the barrier Hamiltonian is separated into a periodic component containing information on the bulk band structure and a non-periodic component containing information on band bending near the interface, electron-electron interactions outside the material and applied fields. After this separation the electronic Schrödinger equation can be reformulated in the effective mass method. The barrier Hamiltonian is

$$\hat{H}_{barrier} = \hat{T}_e(\mathbf{r}) + V_{ee}(\mathbf{r}) + V_{es}(\mathbf{r}) + V_{ext}(\mathbf{r}) \quad (1)$$

with the electron-electron interaction potential  $V_{ee}(\mathbf{r}) = V_d(\mathbf{r}) + V_{xc}(\mathbf{r})$  and the electrostatic potential  $V_{es}(\mathbf{r}) = E_{band}(\mathbf{r}) + V_I(\mathbf{r})$ , where  $V_d(\mathbf{r})$  is the electrostatic dipole potential,  $V_{xc}(\mathbf{r})$  is the exchange-correlation potential,  $E_{band}(\mathbf{r})$  is the energy band levels, and  $V_I(\mathbf{r})$  is the electrostatic potential due to ionized impurities. For a metal occupying  $-\infty < z \leq 0$  an approximate form for the exchange-correlation potential is the electrostatic image potential [REF],  $V_{image}(z) = -\frac{q^2}{16\pi\epsilon_0 z}$ , for  $z \geq z_{im} > 0$ , such that

$$V_{xc}(z) \cong V_{xc,im}(z) = \begin{cases} 0 & z < z_{im} \\ V_{image}(z) & z \geq z_{im} \end{cases} \quad (2)$$

where  $z_{im} > 3\text{\AA}$  generally.

The tunneling current density for an emitted electron is represented as

$$\mathbf{J} = nq\mathbf{v}_{avg}T \quad (3)$$

where  $n$  is the electron density,  $q$  is the electron charge,  $\mathbf{v}_{avg}$  is the average electron velocity, and  $T$  is the tunneling transition probability for the electron traversing the barrier<sup>9</sup>. Two general methods of solving for the tunneling current density have been developed, perturbation and scattering solution methods. The Transfer Hamiltonian method is a perturbation approach that can include many body effects, but it is limited to weak perturbations to the barrier Hamiltonian such that the tunneling probabilities must be very small, this method is used most commonly in scanning tunneling microscopy (STM) experiments and analyzing superconducting tunnel junctions<sup>10</sup>. The Green's function method is a scattering state method that can incorporate many-body interactions, however it is hard method to implement, it is commonly used in STM experiments and the analysis of nanoelectronic structures<sup>11</sup>. The wave function method is a scattering stationary state

method that is not limited to small perturbations to the barrier Hamiltonian, but it is limited to independent electron models, it is the preferred method in Field Emission studies and is the basis for the Fowler-Nordheim formalism<sup>9</sup>.

### 1.3. Field Emission Formalism

In conventional Fowler-Nordheim theory the following are assumed:

- a. the emission process acts adiabatically
- b. the tunneling process is a one-electron process
- c. the tunnel system is large
- d. only electrons moving perpendicular to the interface can tunnel through.
- e. tunneling only occurs from the source to the collector

From these assumptions the Field Emission current density for a particle incident perpendicular to the interface in the direction  $z$  and with energy  $E_z$  is

$$J_z = \frac{q}{h} \int_{-\infty}^{\infty} dE_z T(E_z) n(E_z). \quad (4)$$

Using the WKB representation of the tunneling probability

$$T(E_z) = \exp\left(-\frac{2\sqrt{2m}}{\hbar} \int_{x_1(E_z)}^{x_2(E_z)} \sqrt{V(x) - E_z} dx\right), \quad (5)$$

for a metal cathode at 0K with a triangular barrier potential, as shown in Figure 1, the field emission current density is<sup>8</sup>

$$J_z(F) = A \frac{F^2}{\phi} \exp\left(-\frac{B\phi^{3/2}}{F}\right) \quad (6)$$

where  $F$  is the applied field,  $\phi$  is the metals work function and  $A$  and  $B$  are constants. Small variations in the applied field lead to large changes in the current density and from the field emission current begins to become appreciable at surface electric fields approaching 1V/nm.

From experimental data one obtains the integrated current,  $I(V)$ , as a function of the applied bias,  $V$ . If this data is plotted as  $\ln(I/V^2)$  vs.  $1/V$ , the resulting curve, known as a Fowler Nordheim plot, is a straight line if Field Emission is the dominant emission mechanism<sup>12</sup>. If Field Emission is the dominant mechanism it is assumed that the integrated current is predicted by the current equation

$$I(V) = A_{FN} V^2 \exp\left(-\frac{B_{FN}}{V}\right) \quad (7)$$

where  $V$  is the applied bias. This equation can be linearly transformed into

$$\ln\left(\frac{I}{V^2}\right) = -B_{FN} \frac{1}{V} + \ln(A_{FN}) \quad (8)$$

where the slope of the line is  $S_{FN} = -B_{FN}$  and the intercept is  $I_{FN} = \ln(A_{FN})$ , which are commonly referred to as the Fowler Nordheim parameters. The FN parameters contain information related to the local field enhancement factor and the height of the energy barrier through which the electrons tunnel.

The total energy distribution (TED) of electrons emitted within unit volume and unit time is given by

$$\frac{dJ_z}{dE_z} \propto j_z = n(E) \int_{-\infty}^E T(E_z) dE_z. \quad (9)$$

Contained within this expression is information related to the near surface band structure of the material, such as surface states and bulk band structures. The TED has been used to validate the use of the Fowler Nordheim theory for particular materials, determine specific emission mechanisms and determine relative band edges. It has been found that the theoretical TED fails to predict fine structure present in experimental TEDs, however the theory does correctly predict the overall shape and full width half maximum of the distributions<sup>13</sup>.

#### 1.4. Field Enhancement

Field emission experiments with arrays and metal needles indicate that the emission event is typically localized to a few tips or spots on needles, which emit until a certain current density is reached where by the emitting site is destroyed and the process begins anew at other sites<sup>14</sup>. It was found that this behavior to a large degree can be traced to a modification of the tunneling barrier due to a geometric electrostatic field enhancement effect due to cathode geometry and morphology that results in a significant reduction in the applied electrostatic field required to produce a given field emission current.

The applied electrostatic field is defined as

$$F_0 = V_0/d_{\parallel} \quad (10)$$

where  $V_0$  is the applied bias and  $d_{\parallel}$  is the distance between the anode and cathode structures when the structure is abstracted as a parallel plate capacitor,. The local electrostatic field is defined as

$$F(\mathbf{r}) = \gamma(\mathbf{r})F_0 \quad (11)$$

where the field enhancement factor  $\gamma(\mathbf{r})$ , or in some references  $\beta(\mathbf{r})$ , is a dimensionless surface function that accounts for the effects of the microscopic and macroscopic geometry of the cathode and the cathode-anode system. The field enhancement factor is inversely related to the radius of curvature of the emitting structure.

Due to this behavior the reduction of the radius of curvature of the emitting site is commonly applied to improve the field emission characteristics of cathodes. However as the radius of curvature of the emitting surface approaches nanometer scales the local electric potential that the electron tunnels through can become nonlinear and the turn field can increase<sup>8</sup>. It has also been found that metal insulator vacuum triple junctions can also produce an effect much like geometric field enhancement<sup>15</sup>.

### 1.5. Material effects

The choice of material for a Field Emission cathode affects the maximum theoretical emission current, the efficiency of the emission process and the reliability of the cathode. The electronic structure of the emitting material determines the electron supply that is available for emission, material induced barrier potential modifications impact the efficiency and characteristics of the Field Emission process, and thermal properties of the material affect cathode reliability<sup>8</sup>.

For metals the electron supply is determined by only the Fermi level since the conduction band edge is significantly below the Fermi level, typically 10eV, where the emitted theoretical maximum current density is approximately  $2-3 \times 10^{-3} \text{ A/nm}^2$ . For insulators the electron supply is determined by the electron affinity and location of the band edge for a partially filled conduction band, dopants, surface states and band gap states.

The barrier potential for emission from metal and insulator materials is typically modified by the addition of an image charge approximation to the exchange-correlation potential. The addition of surface adsorbates can affect the tunneling barrier potential for both metal and insulator materials by modifying the surface and in the case of singly adsorbed atoms introducing resonant tunneling structures<sup>13</sup>. For insulator materials the presence of space charge near the emission surface due to dopants or surface band alignment can significantly perturb the barrier potential, possibly introducing surface quantum wells and affecting electron transport and consequently electron emission<sup>5</sup>.

### 1.6. Thermal effects

One of the primary factors affecting the reliability and performance of field emission devices is thermal degradation of cathodes. Thermal instabilities resulting in modification and destruction of the cathode lower the theoretical maximum emitted current density, from  $10^{-7} \sim 10^{-3} \text{ A/nm}^2$ . This modification occurs via field enhanced surface migration of material resulting in surface morphology changes, while destruction takes the form of melting of the cathode and the initiation of a vacuum arc. The thermal conductivity of the emissive material affects the maximum attainable single tip current densities before the cathodes are destroyed. Diamond cathodes can attain current densities much closer to their theoretical maximum compared to metal cathodes, since diamond has one of the largest known thermal conductivities<sup>8</sup>.

The emitter structure is affected by two thermal processes: Joule and Nottingham effect heating. Joule heating primarily affects the emitter volume while the Nottingham

effect is a purely quantum mechanical energy exchange process that affects the emitter surface region.

Initially during the field emission process Nottingham effect heating dominates but after some time Joule heating can dominate, as seen in Figure 2. In nanometer scale micro-protrusions the characteristic size of the emitting structure can be smaller than the electron-phonon mean free path indicating that the emission process is limited only by the Nottingham effect and electron thermalization may not occur, resulting in no Joule heating and relatively high maximum current densities.

### **1.7. Field Emission Applications**

Comparing the characteristics of Solid State and Vacuum Microelectronic devices, as shown in Table I, it is noticed that vacuum is a superior transport medium compared to solids, however space charge limitations on the maximum achievable current density and the fact that only one type of charge carrier is active limit VME applications. Electron beam devices that exploit the vacuum transport environment are the primary application for Field Emission devices. Electron beam devices have been used for application such as flat panel displays, electron microscopy, probe microscopies, microwave tube devices, e-beam lithography, pressure sensors, and space propulsion.

### **1.8. Fabrication of Field Emitters**

The method of field emitter fabrication is dependent on the operational characteristics required by the application, such that there has been a steady development of fabrication techniques that are geared towards certain goals. Field emitters were fabricated in the 1930s

by etching single refractory metal wires, such as Mo and W, for use in electron microscopies. Later in the 1950s arrays of these etched needles were mechanically constructed for use in applications, such as microwave devices. Micro fabrication techniques from the electronics industry was used in the 1960s to develop arrays of gated and un-gated metal tips grown on a single substrate, which became the conventional fabrication method for electronic devices, such as flat panel displays and microwave tubes. In the 1970s arrays of gated and un-gated silicon needles were fabricated. Various coatings or thin films were applied to these field emitter cathodes to improve field emitter performance. To improve reliability of the cathodes current limiting structures, such as ballast resistors and MOSFETs, were incorporated into the fabrication process, substantially increasing the cost to fabricate the cathodes. As shown in Table II the fabrication cost and complexity of these designs increased over time. Beginning in the 1990s newer lower cost processes for field emitter cathodes were developed involving the deposition from solution of materials, for example of CNTs, CNFs and DNPs, and the design of new device structures.

### **1.9. Summary**

As low-dimensional materials increasingly are used in the design field emitter cathodes and likely any electronic device that utilizes them as a field affected tunnel junction it is increasingly important to understand the parameters affecting device characteristics and predict their impact. The size, shape, and morphology of these materials can affect the characteristics of such field emitter cathodes, determining the optimum fabrication method incorporating these materials. This research will focus on the effects of size, shape and

morphology on the field emission characteristics of low-dimensional materials used in efficient fabrication techniques for field emitter cathodes.

### 1.10. References

- <sup>1</sup> V.V. Zhirnov, W.B. Choi, J.J. Cuomo, J.J. Hren, *Applied Surface Science*, **94-5**, 123, (1996).
- <sup>2</sup> V.V. Zhirnov, E.I. Givargizov, P.S. Plekhanov, *Journal Of Vacuum Science & Technology B*, **13**, 418, (1995).
- <sup>3</sup> D. Temple, W.D. Palmer, L.N. Yadon, J.E. Mancusi, D. Vellenga, G.E. Mcguire, *Journal Of Vacuum Science & Technology A*, **16**, 1980, (1998).
- <sup>4</sup> V.P. Mammana, D. Jaeger, O. Shenderova, G.E. Mcguire, *Journal Of Vacuum Science & Technology A*, **22**, 1455, (2004).
- <sup>5</sup> R.G. Forbes, *Solid-State Electronics*, **45**, 779, (2001).
- <sup>6</sup> W.B. Choi, Y.W. Jin, H.Y. Kim, S.J. Lee, M.J. Yun, J.H. Kang, Y.S. Choi, N.S. Park, N.S. Lee, J.M. Kim, *Applied Physics Letters*, **78**, 1547, (2001).
- <sup>7</sup> W.B. Choi, J.J. Cuomo, V.V. Zhirnov, A.F. Myers, J.J. Hren, *Applied Physics Letters*, **68**, 720, (1996).
- <sup>8</sup> G. Fursey, *Field Emission In Vacuum Microelectronics*, (Kluwer Academic, New York, 2005).
- <sup>9</sup> C.B. Duke, *Tunneling In Solids*, (Academic Press, New York, 1969).
- <sup>10</sup> R. Ramprasad, L.R.C. Fonseca, P. Von Allmen, *Physical Review B*, **62**, 5216, (2000).
- <sup>11</sup> R. Lake, S. Datta, *Physical Review B*, **45**, 6670, (1992).
- <sup>12</sup> R.G. Forbes, *Journal Of Vacuum Science & Technology B*, **17**, 526, (1999).

- 
- <sup>13</sup> A. Modinos, *Field, Thermionic, And Secondary Electron Emission Spectroscopy*, (Plenum Press, New York, 1984).
- <sup>14</sup> R.G. Forbes, C.J. Edgcombe, U. Valdre, *Ultramicroscopy*, **95**, 57, (2003).
- <sup>15</sup> M.S. Chung, B.G. Yoon, P.H. Cutler, N.M. Miskovsky, *Journal Of Vacuum Science & Technology B*, **22**, 1240, 2004.
- <sup>16</sup> R. Gomer, *Field Emission and Field Ionization*, (American Institute of Physics, New York, 1993).
- <sup>17</sup> V.V. Zhirnov, L. Bormatova, E.I. Givargizov, P.S. Plekanov, U.T. Son, A.V. Galdetsky, B.A. Belyavsky, *Applied Surface Science*, **94/95**, 144 (1995).
- <sup>18</sup> R.N. Thomas, R.A. Wickstro, D.K. Schroder, H.C. Nathanson, , *Solid-State Electronics*, **17**, 155 (1974).
- <sup>19</sup> D. Temple, *Materials Science And Engineering*, **R24**, 185, (1999).
- <sup>20</sup> Y.S. Choi, J.H. Kang, H.Y. Kim, et. al., *Applied Surface Science* **221**, 370 (2004).
- <sup>21</sup> D. Kang, V.V. Zhirnov, R.C. Sanwald, et al., *Journal Of Vacuum Science & Technology B*, **19**, 50 (2001).
- <sup>22</sup> W.B. Choi, J.J. Cuomo, V.V. Zhirnov, et al, *Appl. Phys. Lett.*, **68**, 29 (1996).
- <sup>23</sup> Intel, :<http://intel.com/education/makingchips/multiple.htm>.

Table I. General Properties of Solid-State and Field Emission Devices

Properties	Solid-State Devices	Field Emission Devices
Current Density (A/cm <sup>2</sup> )		Much smaller
Applied Voltage (V)		Much larger
Structure	Solid/solid interface	Solid/vacuum interface
Charge of Involved Carrier(s)	+ and -	+ or -
Electron transport		Superior
Noise		
Thermal and Shot		Comparable
Flicker	Surface/interface	Worse
Electron energy (eV)		Much greater
Cut-off frequency (GHz)		Larger
Output Power		Larger
Radiation hardness		Much Better
Temperature sensitivity (°C)	-30 to 50	<500

Table II. Processes used for fabrication of specific emitter structures, including the approximate number of masks, total fabrication steps and amount of energy and material required.

Type	Tip Process	# Masks	# Steps	Energy Budget	Ref
Needle	Etched	0	3	Low	16
Tip array	Etched	0	5	Low	17
Tip Array	Etched	1	10	Medium	18
Gated Tip	Grown	2	50	High	19
Gated Tip	Etched	6	80	High	19
Coated Gated Tip	Grown	6	90	High	19
Back-Gate	Grown	2	20	High	20
Coated Needle	Grown	0	8	Medium	21
Coated Needle	Deposited	0	6	Low	22
Back-Gate	Deposited	1	15	Medium	4
Mosfet IC		30	250	Very High	23

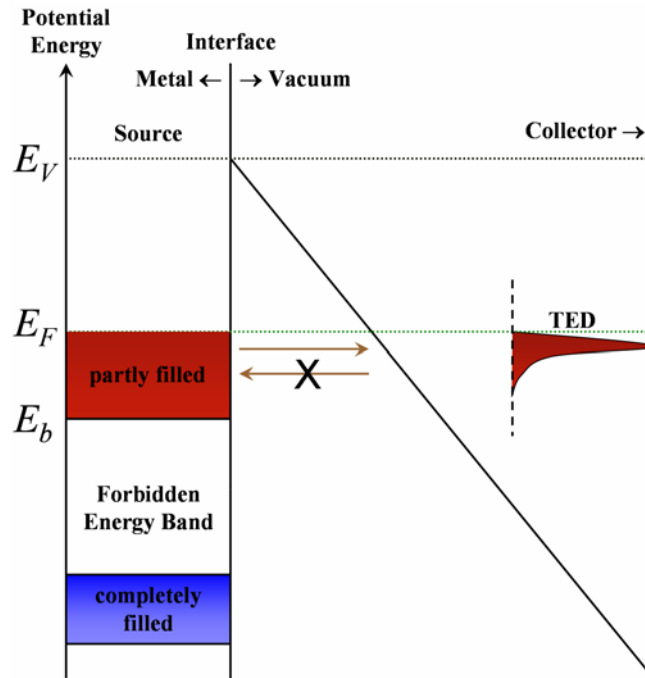


Figure 1. Conventional Fowler Nordheim emission from the partially filled conduction band of a metal cathode source into a collector through a triangular barrier potential. Current from the collector to the source is considered negligible. Electron emission is peaked near the Fermi level as shown in the schematic TED.

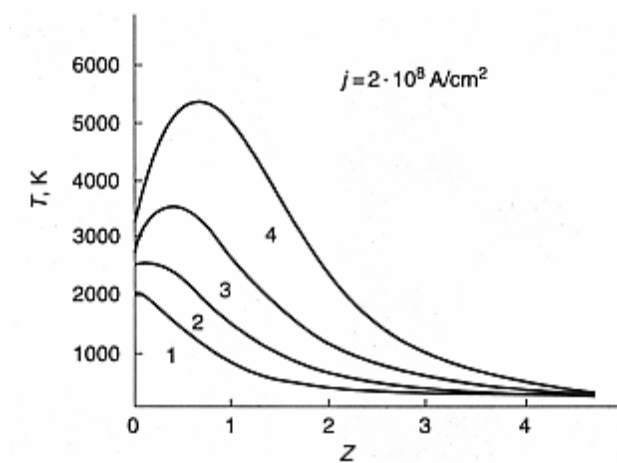


Figure 2. Temperature along the axis of an emitter for times 1,2,3,4; where  $t_1 < t_2 < t_3 < t_4$ .

**Chapter 2. Local electrostatic effects of surface structure on field emission:**

**Metal on metal composite cathodes**

by

D. L. Jaeger and J. J. Hren

Department of Materials Science and Engineering, North Carolina State University, Raleigh,

NC 27695-7907

and

V. V. Zhirnov

Semiconductor Research Corporation, Research Triangle Park, North Carolina 27709-2053

published in

Journal of Applied Physics 93 691 (2003)

## 2.1. Abstract

We examined the classical electrostatic effects due to geometric surface structures on conductive field emission needles numerically using the finite element method (FiEM) and compared our results to several commonly applied analytic relations. Analysis of the morphology of electrochemically prepared Mo needles by high-resolution transmission electron microscopy (HRTEM) was incorporated in the numerical analysis in the form of small surface protrusions and gross needle shape. We found that the error between the electrostatic potential defined by popular analytic equations and both analytic equations derived in prolate spheroidal coordinates and FiEM results was significant for ellipsoidal needles with and without surface protrusions. The morphology of the surface protrusion was found to introduce a significant nonlinear potential barrier near the needle surface. Finally we numerically analyzed a non-symmetric, non-homogeneous experimental needle indicating that even larger errors in the electrostatic potential can be expected relative to analytic equations.

## 2.2. Introduction

It might seem surprising, but there are several unknowns in “classic” electrostatic problems related to field emission. The first and most important unknown is the interaction of the electrostatic field with the inhomogeneous geometry of the realistic emitting surface. This interaction typically cannot be solved as a closed, analytic solution with any degree of accuracy; therefore sophisticated numerical methods such as the Charge Simulation Method,<sup>1</sup> Image Charge Method,<sup>2</sup> Boundary Element Method,<sup>3</sup> Finite Difference Method<sup>4</sup> and the Finite Element Method<sup>5</sup> are required. Ignoring the exact morphology of the field emission

structure is a common practice in the experimental field emission community. The magnitude of the electrostatic field at the emitting surface is estimated using idealized geometrical parameters and rough analytical approximations; e.g.  $F \cong V/5r$  for field emission microscopy (FEM) geometry,<sup>6</sup> or  $F=(h/r)F_0$  for planar geometry.<sup>7</sup> More complicated analytical relations have been derived for idealized structures, such as ellipsoids,<sup>8,9</sup> hyperboloids,<sup>10</sup> prolate spheroids,<sup>11</sup> and for gated<sup>10</sup> and ungated<sup>12</sup> arrays of emitters. However, these relations suffer from an inability to account for geometrical and material irregularities that perturb the morphology from the simple geometries that these relations were derived to solve.

The resolution of a scanning electron microscope (SEM) is insufficient to resolve all features that affect emission; e.g. surface morphology, grain boundaries, adsorbates, and inclusions on the order of several nanometers. Thus using these simple approximations without taking into account the nanostructural composition and morphology of the device can lead to physically erroneous conclusions. A very common attempt at an explanation of anomalous data in the published literature refers to “difficult data”, i.e. referring to hypothetical and *invisible protrusions* (whose effect is in-turn calculated using simplified equations). Thus a common weakness of many field emission measurements is the lack of combined studies employing HRTEM to accompany the field emission data. In particular, no systematic HRTEM studies *before and after field emission* have been published that attempt to detail the changes in morphology accompanying the emitter’s “life” and attempting to determine whether these changes can be correlated with specific events observed during emission.

Understanding the electrostatic field and its interaction with matter is clearly a fundamental question of great significance to the field emission community. You would expect that after 200+ years of development, that the fundamental questions of how the electrostatic field interacts with metallic needles would be answered. On the contrary, many such questions have been debated by the field emission community over several decades but still not adequately addressed. One such fundamental question is whether observed emission phenomena are due to irreversible changes, e.g. in the shape and morphology of the emitting structure by the formation of nanometer-scale protrusions. Another related and fundamental question is how to define the emission area. Recently, Richard Forbes argued that derivation of the emission area using simple models, such as  $\alpha \approx r^2$ , is inaccurate for fundamental physical reasons, and gives values much smaller than the physical area from which electrons are emitted,<sup>13</sup> The community is therefore will aware of problems caused by electrostatic field effects and efforts underway to develop more accurate models for the analyses of field emission experiments.

At what point does the continuum Poisson/Laplace electrostatic approach prove to be less accurate than the discrete atomistic electrostatic approach? The sensitive character of electric fields to the local structure of the metal surface leads to a desire to know the structure of the surface of the emitter/substrate at several scales; that is, structures that affect the far field, intermediate field, and near field behavior. The gross dimensions of the structure are in the mm- $\mu$ m size range and can be characterized using optical microscopy, which then determines the gross magnitudes of the fields. Structures in the  $\mu$ m-10nm range, which can be characterized by SEM, strongly influence fields in the intermediate scale, and are localized near the emitting surfaces. Atomic and molecular scale geometric structures also

determine field enhancement very near a metal surface and can only be resolved by HRTEM, and thus determine unambiguously whether some “exotic” or unexpected localized event is dominating the emission process.

In this paper the electric field on an emitting surface was numerically calculated based on the exact geometry of the tip as determined from HRTEM analysis. Field enhancement effects due to aspect ratios, curvature, and multistage structures were modeled using the Finite Element Method and compared to the analytical models most often used to analyze experimental data. Four specific areas of experimental interest were considered in this work: (1) Idealized Single Tip Field Enhancement Effects, (2) Array Tip Density Electrostatic Effects, (3) Multistage Field Enhancement Effects, and (4) Field Enhancement Effects at experimental tips with inhomogeneous geometry.

### **2.3. Simulation and Method**

The field emitter structures were modeled as a parallel plate vacuum diode with grounded single or multiple tip cathode structures of high aspect ratio and a positively biased anode, as shown in Figure 1. High-resolution transmission electron microscopy indicated that the needle morphology consisted of a base metal substrate with surface asperities that to first order could be modeled as an ellipsoid, as shown in Figure 2. Surface asperities on the needle surface were modeled as convolutions of surface ellipses and the base ellipse. The tips were assumed to be ideal metallic structures without adsorbates. Space charge effects in the region between the cathode and anode were not included, since practical current densities examined in field emission experiments are relatively low.

The two dimensional Laplace's equation in Cartesian coordinates for a source charge free homogeneous medium,

$$\nabla^2 V(x, y) = \frac{\partial^2 V(x, y)}{\partial x^2} + \frac{\partial^2 V(x, y)}{\partial y^2} = 0 \quad (1)$$

was used to analyze the field distributions for asymmetrical morphologies and arrays of tips, using the corresponding Dirichlet boundary conditions for constant voltage surfaces,  $V(\vec{r}) = V_{\text{applied}}$ , and the Neumann boundary conditions for symmetry axes,  $\nabla V(\vec{r}) = 0$ , as illustrated in Figure 1. Single tip field enhancement was analyzed in three dimensions using a cylindrical transformation of the two dimensional numerical domain into the three dimensional physical domain of the idealized diode structure. The size of the physical domain was chosen such that effects of electrostatic shielding did not significantly affect the results. Assuming the problem has azimuthal symmetry, Laplace's equation in cylindrical coordinates reduces to:

$$\nabla^2 V(r, z) = \frac{1}{r} \frac{\partial}{\partial r} \left( r \frac{\partial V(r, z)}{\partial r} \right) + \frac{\partial^2 V(r, z)}{\partial z^2} = 0 \quad (2)$$

This allowed a significant reduction in the computational resources required for a three dimensional solution of Laplace's equation on the problem domain. The three dimensional formulation of Laplace's equation also provided a higher order of accuracy in modeling the actual fields experienced by tunneling electrons near a metallic surface. The morphology of the needles modeled was necessarily limited to rotationally symmetric structures and needle density effects in arrays were not modeled.

The finite element method (FiEM) was used to solve the resulting Laplace equation,  $\nabla^2 V(\vec{r}) = 0$ , using the Galerkin weak formulation of the elliptic partial differential equation. A Delauney-Voronoi algorithm generated the unstructured mesh/grid of the two-dimensional

numerical. The computational mesh was adaptively refined in regions where heterogeneities and/or high electrostatic fields existed, providing very dense meshes in these regions which capture the character of the rapid field changes near the surface that are of interest in field emission studies. A significant decrease in the computational cost of solving for the potential and fields, while a high level of accuracy was possible in regions of interest, was achieved in this manner. Laplace's equation was solved for the potential within the numerical domain at the nodes of the generated meshes, with the resulting field strength found by solving Gauss's law,  $E(\vec{r}) = -\nabla V(\vec{r})$ . Linear triangular shape functions were used to construct the linear system of equations that defines the solution in the numerical domain. Dirichlet boundary conditions defined the voltages applied to the anode and cathode surfaces, while Neumann boundary conditions defined the symmetry planes of the numerical domain. The Matlab PDE toolbox<sup>14</sup> was used to construct the adaptively refined computational grid and solve the resulting system of linear equations for the Laplace equation over the domain using the Finite Element Method.

## 2.4. Results and Discussion

### 2.4.1. Idealized Single Tip Field Enhancement Effects

The field enhancement factor for single emitters can be calculated using analytical formulations for simple geometries<sup>7,15-17</sup> and approximated empirically from experimental data for rather complex geometries.<sup>18</sup> We first performed several experiments comparing the potential and electric fields resulting from the analytical expressions for grounded ellipsoidal emitters on infinite parallel plate capacitors and the finite element method approach. Analytical expressions for the electrostatic potential distribution normal to the

needle centroid of a half ellipsoid of revolution on a plane cathode separated from a plane anode was derived by several authors as<sup>8,9,15</sup>:

$$V(z) = E_{\infty} z \left( 1 - \frac{\ln \left( \frac{z + \sqrt{h^2 - r^2}}{z - \sqrt{h^2 - r^2}} \right) - 2 \frac{\sqrt{h^2 - r^2}}{z}}{\ln \left( \frac{h + \sqrt{h^2 - r^2}}{h - \sqrt{h^2 - r^2}} \right) - 2 \frac{\sqrt{h^2 - r^2}}{h}} \right) \quad (3a)$$

Using Gauss's law the field at the ellipsoid apex at an applied anode bias  $V_0$  and anode cathode plate separation  $d$  is:

$$E_0 = \gamma_{3d} \frac{V_0}{d} \quad (3b)$$

where the three dimensional field enhancement factor  $\gamma_{3d}$  and the radius of curvature at the ellipsoid surface along the centroid,  $r_c$ , are:

$$\gamma_{3d} = 2 \frac{(h^2 - r^2)^{3/2}}{hr^2 \left[ \ln \left( \frac{h + \sqrt{h^2 - r^2}}{h - \sqrt{h^2 - r^2}} \right) - 2 \frac{\sqrt{h^2 - r^2}}{h} \right]} \cong \frac{2 \frac{h}{r_c}}{\ln \left( 4 \frac{h}{r_c} \right) - 2} \quad (3c)$$

$$r_c \Big|_{\substack{x=0 \\ y=h}} = \frac{r^2}{h} \quad (3d)$$

The correspondence in field magnification factors between the three dimensional ellipsoidal cylinder and two dimensional ellipsoidal wedge is:

$$\frac{\gamma_{3d}}{\gamma_{2d}} = \frac{2 \sqrt{h/r_c}}{\ln \left( 4 \frac{h}{r_c} \right)} \quad (3e)$$

A further analytical expression for the potential and field normal to the centroid of an arbitrary needle were derived for regions very near the needle surface<sup>17</sup> and formulated as:

$$V(z) = E_{\infty} z \left( \frac{\gamma \cdot r_c^2}{r_c (r_c + z)} + 1 \right) \quad (4a)$$

The numerical approach converged to the analytical results rapidly using adaptively refined meshes in the calculations. The FEM results for coarse meshes that do not reflect the structure of the emitter geometry corresponded well to the analytical results in the intermediate regime between the cathode and anode; however, close to regions of high curvature, where emission is assumed to occur, the numerical results diverged significantly from the analytical results. To overcome this weakness the computational grid was adaptively corrected, resulting in a satisfactory convergence between the analytical and numeric results, as illustrated in Table I. The distance between nodes in the computational mesh near the region of emission was approximately 0.1 nm, an assumed atomic lower limit to the smoothness of the material surface, that gave a satisfactory divergence between the numerical and analytical approaches.

Comparing the numerical and analytical results with a common experimental relation for the field enhancement, as shown in Figure 3 for high aspect ratio structures with small radii of curvature, the experimental relation can overstate the field enhancement effect of the structures geometry by an order of magnitude or more for a simple idealized ellipsoidal structure. The potential in the direction normal to the tip apex surface was calculated using two analytic expressions due to Galdetskiy, Eq. (3a), and Zhirnov, Eq. (4a), respectively and interpolated from the FiEM solution, as shown in

Figure 4, indicating excellent agreement between Galdetskiy's and the FiEM solutions through the entire domain, except very near the needle apex, while agreement between Zhirnov's relation and the FiEM solution occurred only near the needle apex. In

order to correct for this lack of agreement far from the needle apex, Eq. (4a) was modified into the form:

$$V(z) = E_{\infty}(z+h) + E_o \frac{r_c^2(z-d)}{(z+r_c)(r_c+d)} \quad (4b)$$

however this modified functional also does not approximate the FiEM results accurately near the needle apex. This discrepancy near the needle apex between Galdetskiy's rigorously derived potential relation, Eq. (3a), Zhirnov's physically based relation, Eq. (4a), and the modified formula, Eq. (4b), is a result of the physically non ideal structure of the numerical mesh, which is reminiscent of the actual atomic structure of the needle surface, where local atomic scale features perturb the surface geometry from the ideal shapes considered in Galdetskiy's analysis.

The observed divergence between the numerical and analytical results near the metal surface is understandable when examined with respect to the nature of the material surface used in the two approaches. The analytical approach assumes the ellipsoidal metal surface is a continuously smooth surface without any atomic scale features, while the mesh used in the numerical approach is a discretely smooth surface that could be used to represent atomic surface features. The nature of the numerical approach may therefore qualitatively model the electrostatic field disturbances due to the surface atomic lattice, which for features approaching atomic dimension, may not be adequately described as a mathematically smooth surface.

#### 2.4.2. Multistage Field Enhancement Effects

Multistage field enhancement effects encompass regular and random variations in emitter morphology, in which the geometric mismatch between structures determine the

degree of field enhancement.<sup>19-22</sup> Using the preceding information and conditions, we simulated the effects of multiple ellipsoidal asperities present on an ellipsoidal tip. Field enhancement factors for two component structures have been presented as the two step field enhancement approach (TSFE),<sup>23</sup> where

$$E_2 = \gamma_1 E_1 = \gamma_1 (\gamma_0 E_0) \quad (5)$$

If we consider structures consisting of N distinct stages or substructures, which we will refer to as the multistage field enhancement effect, MSFE, the field enhancement factor for these structures has been given as<sup>24</sup>:

$$E = \prod_{i=0}^N \gamma_i E_0 \quad (6)$$

The geometric model of this composite stage needle structure consisted of individual ellipsoids layered on top of each other, largest to smallest, with the centroid of a small ellipse being aligned with apex of a large ellipse. This resulted in angles approaching 0° at the intersection between the two ellipses as  $D_{small} \rightarrow D_{large}$  and approaching 90° as  $D_{small} \ll D_{large}$ , where  $D_R$  is the dimensionality of the structure.

The fields across the emitter surface and near the region of maximum emission are presented in Figure 5. Far from the tip surface the induced potential and electric field distributions approximated the field structure induced by an ideal parallel plate diode under similar conditions; however, near the needle surface the field was strongly influenced by the surface morphology. The electrostatic field distribution across the emitter surface exhibited sharp intensity peaks centered about the surface asperities present on the base emitter and field suppression was observed at the asperity- substrate interface, which has been attributed to the electrostatic screening influence of the asperities.<sup>25</sup> The surface field magnitude

distribution across the apexes of the asperities were continuous and differentiable along with exhibiting the previously described local maximums in field intensity, indicating that field affected deposition processes, such as dielectrophoresis, that are strongly influenced by the magnitude and/or gradient of the localized surface electric field, will preferentially occur in those regions where the magnitude of the field strength or gradient is greatest. The field intensity roughly varies with the geometrical variations between the base tip and the asperities at these locations; however, strong discrepancies arise near the interface regions between the structures.

The agreement between analytic and numeric results for the field enhancement at the site of maximum emission for a two layer geometric system is presented in Figure 6 and Table II. The variation in field intensity about the centroids of these surface structures could increase the maximum fields by an order of magnitude, producing highly localized field enhancement effects around these structures. The geometric agreement between the base structure and asperity has a demonstrative effect on the agreement between the analytic and numerical results. Assuming the geometric mismatch can be quantified as some parameter  $\alpha$ ,  $\alpha \sim 1$  for very significant geometric mismatches and  $\alpha \ll 1$  for slight geometric mismatches.

Multiple asperities layered on top of one another showed a similar trend of increasing the maximum fields induced at the emitter surface, while the relative geometric match between each successive asperity layer on the surface of the emitter affected the magnitude of such enhancement as:

$$E = \left( \prod_{i=1}^N \alpha_i \gamma_i \right) E_0 \quad (7)$$

where  $\alpha_i$  is the degree of geometric mismatch between the asperity and its base, the ideal N-stage field enhancement model corresponds to  $\alpha_i = 1$ . These multistage field enhancement

effects produced maximum fields much less than the ideal N-stage field enhancement mechanism predicts, such that some  $\alpha_i s < 1$ . Simulations show that multiplicative scaling of field enhancement effects of multiple structures mounted on one another does not generally occur for the typical needle structures used in field emission. The effects for a structure of multiple spheres, in which the radii of each sphere is one-half the radii of the previous sphere in which the smaller sphere is embedded, are presented in Figure 7. Assuming that the degree of geometric mismatch is equivalent between each stage, then the MSFE can be expressed as:

$$E = (\alpha^{N-1} \gamma^N) E_0 \quad (8)$$

indicating that the disagreement between the ideal MSFE model and the numeric will scale as the  $N^{\text{th}}$  power. This behavior is indeed observed in the lack of agreement between the MSFE results and FiEM results, where  $\frac{\alpha_{FiEM}}{\alpha_{ideal MSFE}} \approx 0.53$ , indicating that the ideal MSFE model can significantly overstate multistage field effects.

Examination of the potential barrier, which includes Jensen's "analytic" image charge potential,<sup>26</sup> for a small embedded particle on the surface of a relatively large elliptical substrate, Figure 8, shows that the large field enhancement is effective only within a relatively small distance near the surface and the potential is highly nonlinear. Simple approximations using a "standard" image charge affected triangular potential barrier may not prove accurate due to this nonlinear potential barrier, which rapidly diverges from the ideal triangular image affected barrier within 5 Å of the metal surface.

Minimizing the effects of charge screening due to geometric considerations of the structure of these composite structures increases the relative agreement between the ideal and

numeric results, with the best agreement being a base sphere with ellipsoid and spherical asperities. However the maximum field enhancement observed resulted from small, high aspect ratio ellipsoidal asperities on large, high aspect ratio ellipsoidal base tips, where the  $\alpha_{fs} \approx 1$ . Use of a fractal/dendritic surface therefore may not provide nearly as much benefit, as the MSFE model would indicate. The stability of these types of surfaces would also be of concern due to thermal/field-enhanced diffusion and resistive heating of the dendrites, resulting in thermal diffusion or explosive destruction of the dendrites.

#### 2.4.3. Geometrically Inhomogeneous Needle Field Enhancement Effects

An experimental tip, shown in Figure 9, was modeled using a convolution of ellipsoids, which approximated the specific surface structure of the tip, through an examination of the relevant HRTEM micrographs of the tip in question. The structure of the resulting tip used in the simulation and the resulting field distribution for a wedge 2D geometry is presented in Figure 10. The field distribution along the surface of the needle was a maximum at the sharp corner on the left hand side and less intense along the centroid of the tip. A local field maximum along the centroid does not seem intuitive and indicates that it is likely that there is some problem with the approach taken. This problem was isolated to the 2D→3D coordinate transform used in the analysis. A two dimensional examination of this problem, as shown in Figure 10, revealed that the field maximum did occur on the left side protuberance and the strong local field maximum was not observed along the needle centroid. A Fowler-Nordheim analysis of the field emission current from this needle therefore should use the radius of curvature of the protuberance, which was resolved in the HRTEM, and not the tip shape observed using SEM, which appeared to be an

ellipsoidal needle with a radius of curvature determined by the conventional algebraic method.

A “precise” resolution of the 3D fields of irregularly shaped needles requires several micrographs of the needle at different tilt angles to account for the surface inhomogeneities that exist and a true 3D finite element mesh that will not suffer the problems associated with the coordinate transformations. 2D slab solutions of these needles provide qualitative potential/field distribution information, however they do not account for dimensional effects that can have unknown effects.

## **2.5. Conclusions**

In conclusion, we have found that the electrostatics of homogeneous and composite needle structures is not well described by popular analytic approximations. The agreement between analytic and empirical relations with numeric approximation of the electrostatic fields for homogeneous needles indicate that naïve use of empirical relations without considering the specific conditions that they are applicable will lead to grossly inaccurate results. Such practical advice is also applicable to the generally accurate analytic equations that were affected by atomic scale surface irregularities induced by the numerical mesh producing deviations from the numeric results. Simulations of composite needle structures demonstrated that the agreement between the multistage field enhancement model and numerical results is generally very poor; indicating that the dimensional interaction between the various geometric structures that are a part of the composite needle is an important electrostatic factor that significantly affects the surface field and potential barrier. Inhomogeneous field enhancement effects for an experimental needle were investigated,

revealing that local surface structure significantly affects local electrostatic fields, shifting the magnitude and distribution of the fields, and therefore the physical processes influenced by these fields may be significantly altered in scope and intensity by this effect. These nano and mesoscale electrostatic perturbations, which are a function only of geometric parameters of the composite metal structure, are complex phenomena that are extremely difficult to analyze except with the use of sophisticated numerical methods that account for the multiscale nature of these structures. Understanding and quantifying these multiscale effects thus requires nanoscale resolution of the morphology, such as modern high-resolution electron microscopy provides, in concert with sophisticated numerical procedures.

## 2.6. References

- <sup>1</sup> J. Itoh, Y. Tohma, K. Morikawa, S. Kanemaru, and K. Shimizu, *J. Vac. Sci. Technol. B*, **13**, 1968, (1995).
- <sup>2</sup> G. Mesa, E. Dobado-Fuentes, and J.J. Saenz, *J. Appl. Phys.*, **79**, 39, (1996).
- <sup>3</sup> R.L. Hartman, W.A. Mackie, and P.R. Davis, *J. Vac. Sci. Technol. B*, **12**, 754, (1994).
- <sup>4</sup> W.B. Herrmannsfeldt, I. Becker, I. Brodie, A. Rosengreen, and C.A. Spindt, *Nucl. Instrum. Methods Phys. Res. A*, **298**, 39, (1990).
- <sup>5</sup> L.R.C. Fonseca, Paul von Allmen, and R. Ramprasad, *J. Appl. Phys.*, **87**, 2253, (2000).
- <sup>6</sup> R. Gomer, *Field Emission and Field Ionization*, (Harvard Univ. Press, Cambridge, MA, 1961).
- <sup>7</sup> T. Utsumi, *IEEE Trans. Elect. Dev.*, **38**, 2276, (1991).
- <sup>8</sup> H. G. Kosmahl, *IEEE Trans. Elect. Dev.*, **38**, 1534, (1991).
- <sup>9</sup> A. Galdetskiy, *Technical Digest of IVMC'97, Kyongju, Korea*, 598, (1997).

- <sup>10</sup> K.L. Jensen, E.G. Zaidman, M.A. Kodis, C. Hor, P. Mukhopadhyay-Phillips, K. Nguyen and L. Malsawma, *Appl. Surf. Sci.*, **111**, 204, (1997).
- <sup>11</sup> L.H. Pan, T.E. Sullivan, V.J. Peridier, P.H. Cutler, and N.M. Miskovsky, *Appl. Phys. Lett.*, **65**, 2151, (1994).
- <sup>12</sup> J.D. Levine, *RCA Review*, **32**, 144, (1971).
- <sup>13</sup> R.G. Forbes, *Solid State Elect.*, **45**, 779, (2001).
- <sup>14</sup> *Partial Differential Equation Toolbox Users Guide*, The MathWorks, (1996). available at <http://www.mathworks.com/access/helpdesk/help/toolbox/pde/pde.shtml>
- <sup>15</sup> D.A. Kirkpatrick, A. Mankofsky, and K.T. Tsang, *Appl. Phys. Lett.*, **60**, 2065, (1992).
- <sup>16</sup> J. D. Nordgard, *J. Appl. Phys.*, **48**, 3042, (1977).
- <sup>17</sup> V.V. Zhirnov, *J. Phys. IV*, **6(C5)**, 107, (1996).
- <sup>18</sup> C.J. Edgcombe and U. Valdre, *J. Microscopy*, **203**, 188, (2001).
- <sup>19</sup> D. Atlan, G. Gardet, V.T. Binh., N. Garcia, and J. J. Saenz, *Ultramicroscopy*, **42**, 154, (1992).
- <sup>20</sup> V.T. Binh, S.T. Purcell, V. Semet, and F. Feschet, *Appl. Surf. Sci.*, **130-132**, 803, (1998).
- <sup>21</sup> O.B. Isayeva, M.V. Eliseev, A.G. Rozhnev, and N.M. Ryskin, *Solid State Elect.*, **45**, 871, (2001).
- <sup>22</sup> D.Y. Zhong, G.Y. Zhang, S. Liu, T. Sakurai, and E.G. Wang, *Appl. Phys. Lett.*, **80**, 506, (2002).
- <sup>23</sup> V.V Zhirnov, E.I. Givargizov, and P.S. Plekhanov, *J. Vac. Sci. and Techn. B*, **13**, 418, (1995).
- <sup>24</sup> V.A. Solntsev, and A.N. Rodionov, *Solid State Elect.*, **45**, 853, (2001).

- 
- <sup>25</sup> N.M. Ryskin, A.G. Rozhnev, and D.I. Trubetskov, *Technical Digest of IVMC'97, Kyongju, Korea*, 310, (1997).
- <sup>26</sup> K.L. Jensen, *J. Appl. Phys.*, **88**, 4455, (2000).

Table I Degree of agreement between analytical and numerical approaches for various model geometries.

$h(\mu m)$	$r_c (nm)$	$\beta_{FiEM} / \beta_{analytic}$
2	200	1.088
2	20	0.950
2.0	2000	0.988
0.2	200	0.985
0.1	100	0.987
1.1	9.09	0.990
2.2	18.18	0.990

Table II. Percent error between analytic models and numerical results for the maximum field enhancement achievable at the composite needle surface.

Base		Particle		$r_{base}/r_{tip}$	$\gamma_{FIEM}$	$\Delta\gamma/\gamma_{FIEM}$
$r(\mu m)$	$h(\mu m)$	$r(nm)$	$h(nm)$			
2	2	200	200	10	8	15
2	2	0.1	0.1	20	8	11
0.5	0.5	20	220	25	109	57
0.5	0.5	2	22	250	149	15
1	1	2	22	500	149	15
0.2	2.2	20	20	0.01	61	182
0.2	2.2	2	2	0.1	127	34
0.2	2.2	0.5	0.5	0.4	158	9
0.2	2.2	20	220	10	371	778
0.2	2.2	10	110	20	384	748
0.2	2.2	5	55	40	822	297
0.2	2.2	2	22	100	1649	98

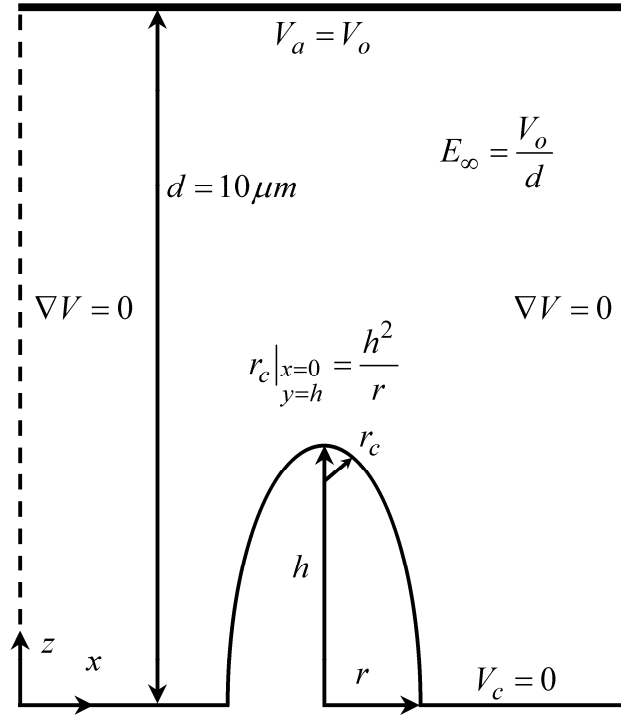


Figure 1. Planar diode geometry with ellipsoidal needle, appropriate boundary conditions approximating the experimental domain modeled and geometrical parameters.

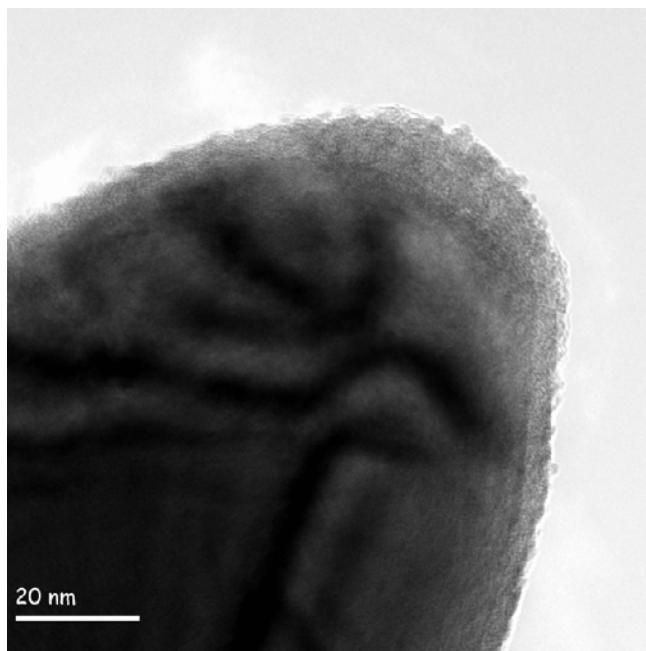


Figure 2. HRTEM profile of an electrochemically etched Mo needle exhibiting a nonhomogeneous profile with many surface features.

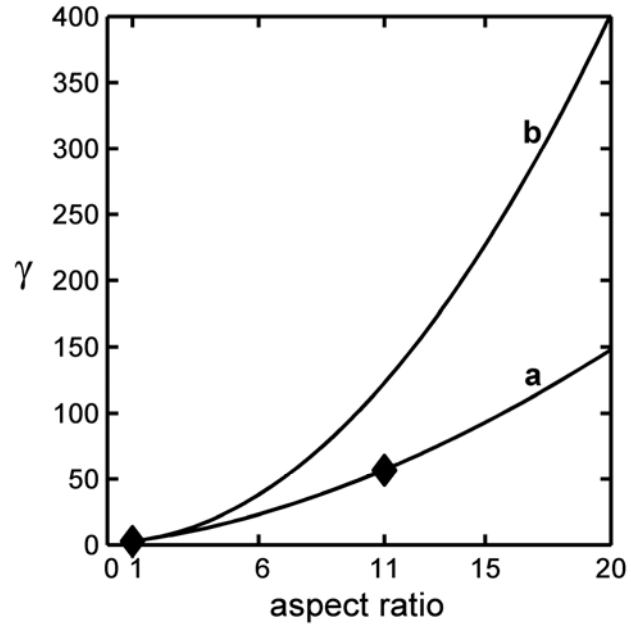


Figure 3. Field enhancement factors versus aspect ratio for ellipsoidal emitters using numeric and analytical methods. (a) exact analytic expression of Eq. (3c), (b) a common experimental approximation,  $\gamma \approx h/r + 2$ , and (diamonds) the FiEM result.

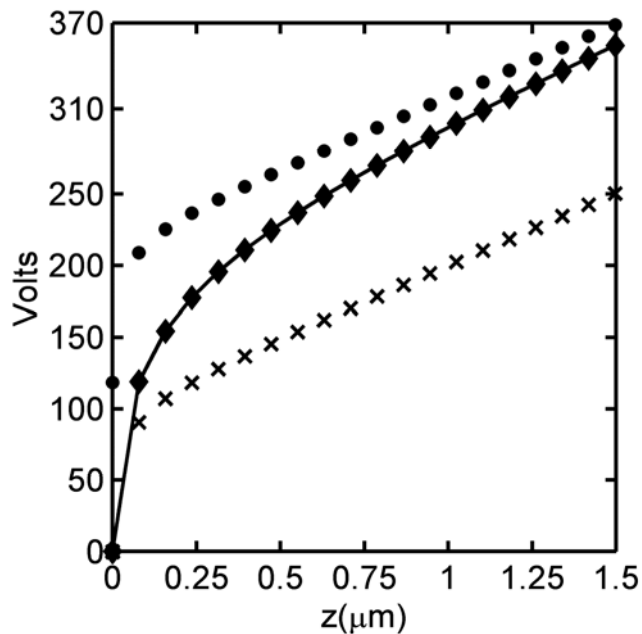


Figure 4. Potential normal to the ellipsoidal needle apex calculated using several methods. (solid line) the FiEM numeric approach, (diamonds) the exact analytic formula Eq. (3a), (crosses) an approximate form of the potential given by Eq. (4a), and (circles) the modified formula of Eq. (4a) given by Eq. (4b).

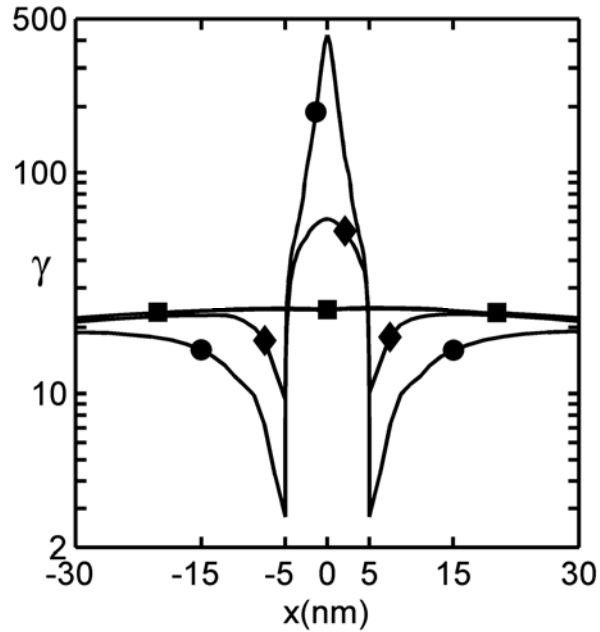


Figure 5. Field enhancement across the emitter surface for a two stage composite needle. (squares) a base needle with  $r_c = 200\text{nm}$ , (diamonds) a protrusion with  $r_c = 3\text{nm}$  on the surface of the base needle, and (circles) a protrusion with  $r_c = 0.625\text{nm}$  on the surface of the base needle.

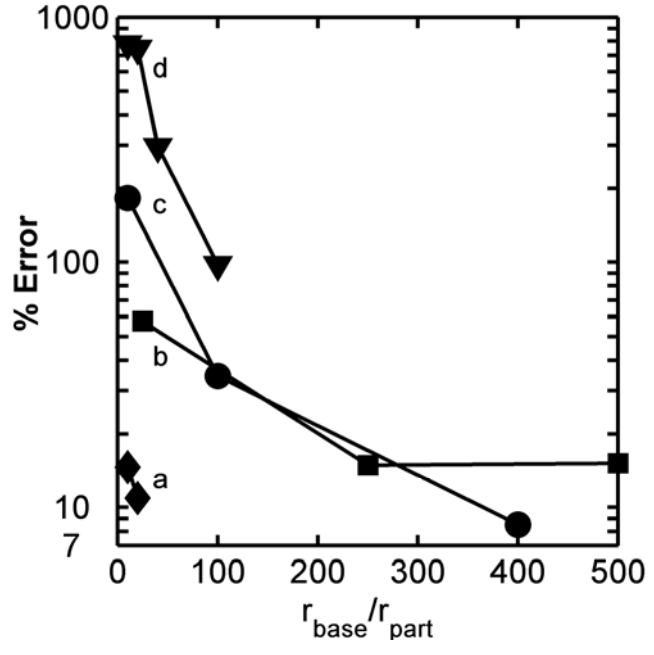


Figure 6. Percent error between the MSFE model and numerical results using the Finite Element Method for various types of idealized inhomogeneities on elliptic and spherical needle substrates. (a) spherical particle embedded on spherical substrate, (b) ellipsoidal particle embedded on spherical substrate, (c) spherical particle embedded on ellipsoidal substrate, (d) ellipsoidal particle embedded on ellipsoidal substrate.

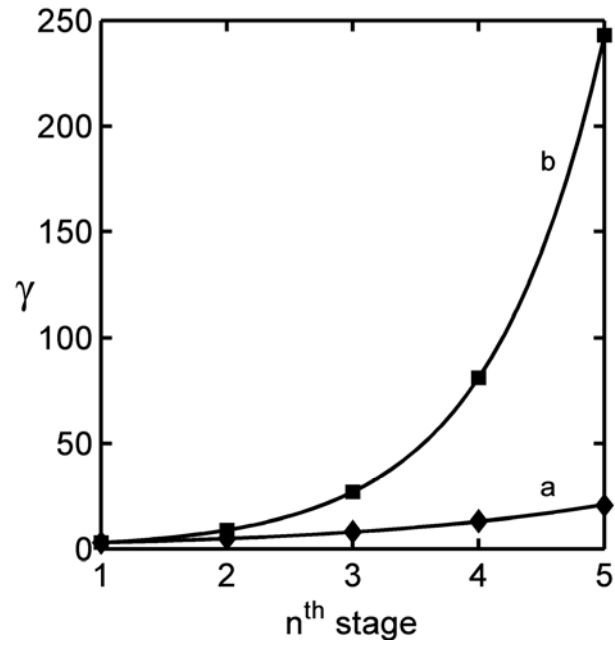


Figure 7. Field magnification values as a function of the number of substructures consisting of embedded spheres of decreasing radii. (a) FiEM numeric results, (b) results of the ideal MSFE model using Eq. (6).

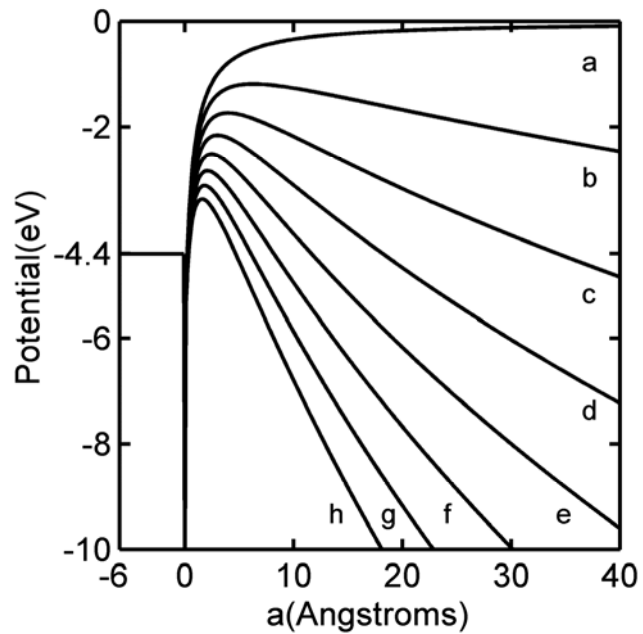


Figure 8. Potential profile of a composite metal needle using FiEM numeric results. Applied anode voltages of (a) 0V, (b) 100V, (c) 200V, (d) 300V, (e) 400V, (f) 500V, (g) 600V, and (h) 700V.

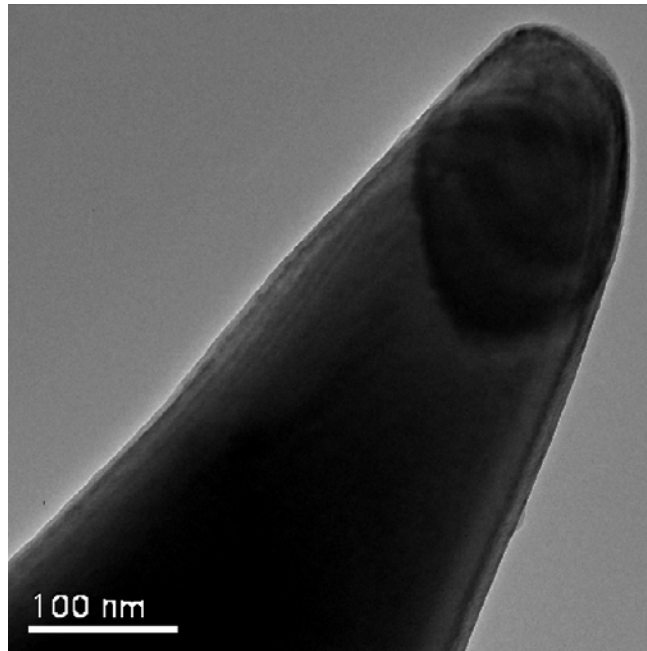


Figure 9. HRTEM image of the simulated needle.

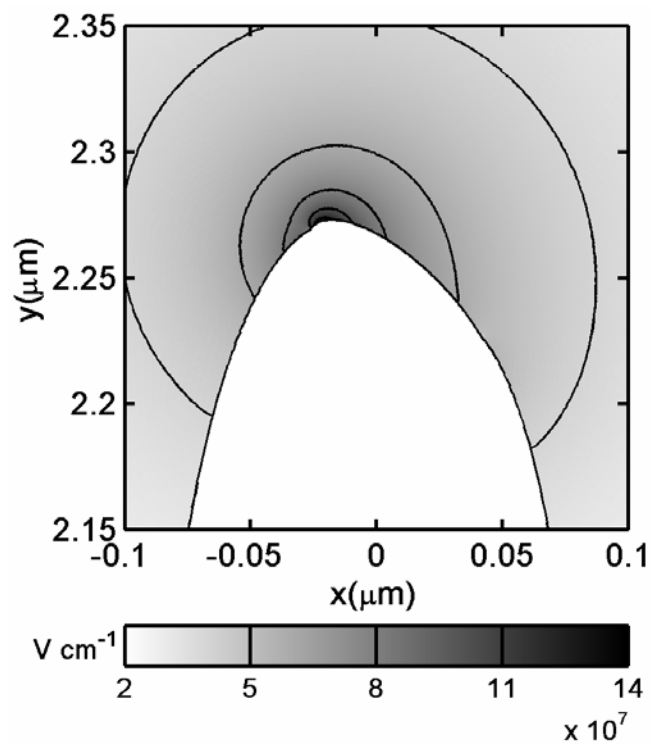


Figure 10. The geometric approximation of Figure 9 and the resultant field distribution.

**Chapter 3. Electrostatic effects of conformal and isolated diamond  
nanodots on field emission**

by

D. L. Jaeger and J. J. Hren

Department of Materials Science and Engineering, North Carolina State University, Raleigh,  
NC 27695-7907

and

V. V. Zhirnov

Department of Materials Science and Engineering, North Carolina State University, Raleigh,  
NC 27695-7907 and

Semiconductor Research Corporation, Research Triangle Park, North Carolina 27709-2053

Submitted to

Applied Physics Letters

### 3.1. Abstract

Extraction and analysis of reliable data from field emission measurements of needle structures with diamond coatings is a vexing and complex problem, but of great importance in understanding the electron emission mechanism. The electrostatic fields of diamond/metal composite needle structures were numerically analyzed based on experimental input describing their exact geometry and chemical composition. We demonstrate in this article an expectation that electrostatically influenced emission and particle transport properties differentiate bare metal needle substrates, metal needles with nonconductive coatings of isolated particles, and metal needles with continuous coatings of nonconductive films. This behavior partially explains the existence of “anomalous” and “normal” thickness effects experienced by systems of diamond coatings.

### 3.2. Introduction

Composite field emitters consisting of a conductive needle substrate with coatings of wide band gap materials (e.g. diamond, AlN, etc.) have been studied extensively over the past few years<sup>1,2,3,4</sup>. It was found experimentally that such coatings offer improvements of emission properties over their metallic needle-shaped emitter substrates. However, the mechanism of electron emission in such structures is not completely understood, because they are complex. The existence of surface charge, new interfaces, material inhomogeneities, and/or doping can have dramatic effects on the emission behavior of these composite emitters.

The thickness and size dependence of metal-nanodiamond composite needle structures have a significant and generally non-intuitive impact on field emission.

Experimentally the emission voltage of emitters coated with diamond<sup>5</sup> and AlN<sup>6,7</sup> films, with a thickness greater than 20-50 nm, was observed to decrease (relative to the film thickness, as the film thickness decreased). These observations are sometimes referred to as the “normal” thickness effect. Such behavior has typically been associated with the resistive voltage drop across the films or to negative space charge within the insulating coating. One might project that this trend would continue with even thinner diamond coatings, the ultimate limit being a single, isolated particle that would exhibit optimum emission properties. Later studies with much thinner diamond and AlN deposits on metal needles indicated that the emission voltage was substantially increased, contradicting the previous predictions of the “normal” thickness effect<sup>6,7</sup>, therefore we refer to this latter behavior as the “anomalous” thickness effect<sup>8</sup>. This thickness dependent emission behavior exhibited emission properties that were at an optimum for relatively thin continuous films, where the “anomalous” thickness effects are assumed to appreciably influence the emission process.

Models of the emission mechanisms of such structures involve assumptions that significantly affect their valid analysis. We have striven to reduce such assumptions to a minimum, so that we can derive a quantitative model for their field emission behavior. Theoretical efforts should be based on solid experimental input therefore the results presented in this work were obtained for an actual composite diamond-metal tip system characterized by high resolution transmission electron microscopy before and after field emission measurements<sup>9</sup>.

We report on the use of classical electrostatic simulations to elucidate those electrostatic phenomena that have a significant impact on field emission from nanodiamond coated molybdenum needles. Through the use of high-resolution transmission electron

microscopy (HRTEM) and electron energy loss spectroscopy (EELS), before and after emission, the exact geometry and chemical composition of the composite cathodes was determined. We previously used a similar approach in the electrostatic analysis of metal needles exhibiting geometric perturbations from ideal shapes, showing that analytic methods are often not accurate and lead to erroneous analyses<sup>10</sup>. The local electric potentials and fields at the emitting surfaces were numerically calculated using morphological and compositional physical information derived from this data.

### 3.3. Experimental Input

Field emission experiments carried out on metal- nanodiamond coated needles exhibit a thickness dependent shift of the threshold voltage and current evolution with applied bias<sup>9</sup>. The field emission characteristics generally improve as the film thickness decreases: however, we have consistently observed an “anomalous” thickness dependence for very thin coatings, including one consisting of a single isolated nanodiamond particle ( $d \approx 5$  nm)<sup>9</sup>. For such nanometer dimension coatings, emission characteristics are degraded, by comparison with the emission observed from the same bare metallic needle. Such anomalous thickness dependent field emission behavior is not confined to nanodiamond coatings, it has been also observed in metal field emitters with AlN coatings<sup>1,2</sup>. Such counter-intuitive behavior suggests that some size-selective mechanisms take place at or below a critical coating thickness.

The morphology and chemical composition of the composite metal nanodiamond coated needles were characterized using HRTEM and EELS. The results can be summarized as follows:

- 1) HRTEM of typical as prepared needles indicates strong deviations from ideal geometric structures.
- 2) No traces of a graphite phase were found in any nanodiamond clusters before field emission using HRTEM and EELS analysis<sup>9</sup>.
- 3) HRTEM did not reveal any measurable changes in the metal substrate geometry that could account for the observed changes in emission after both nanodiamond deposition and field emission.

From HRTEM of a Mo needle with a coating of discrete isolated nanodiamond particles, the particles appear to be embedded in the Mo substrate at or near the region of minimum radius of curvature following field emission and are ‘spherical’ in shape with radii of approximately 2.6 nm<sup>9</sup>.

### 3.4. Numerical Method

Bulk diamond physical parameters were assumed throughout the numerical analysis of the Mo-diamond nanodot needles. The nanodiamond particles were assumed to be insulating and that surface charge could be neglected. The three dimensional classic electrostatic field of the structures was analyzed using finite element method solutions to Laplace’s equation. Isoparametric linear elements, an unstructured, adaptively refined computational mesh and the axisymmetry of the physical domain was utilized in the finite element analysis as in our previous study of bare metal needles<sup>10</sup>.

### 3.5. Results and Discussion

The thickness dependent emission behavior of these wide band gap semiconductor coated metal needles can generally be expressed as:

$$I(r, V, \beta) = I_{\text{normal}}(r, V, \beta) + I_{\text{anomalous}}(r, V, \beta) \quad (1)$$

where  $r$  is the “thickness” of the coating,  $V$  is the applied bias and  $\beta$  accounts for other parameters affecting the emitted current. An optimum thickness of the wide band gap coating,  $r_{\text{optimum}}$ , was observed where by the most favorable emission properties were realized.

This behavior indicates that to leading order the emission current can be described as:

$$I(r, V, \beta) \approx \begin{cases} I_{\text{anomalous}}(r, V, \beta) & \text{if } r < r_{\text{optimum}} \\ I_{\text{normal}}(r, V, \beta) & \text{if } r > r_{\text{optimum}} \end{cases} \quad (2)$$

where the emission mechanisms and processes of the “anomalous” and “normal” emission dependencies must exhibit some fundamental differences.

Embedded nanoparticles exhibited a strong triple-junction effect at the metal insulator vacuum (MIV) junction of the metal nanodiamond composite needle. Such triple junctions have been recognized to be an important component in field emission from diamond particulate films<sup>3</sup>. The electric field distribution near the nanodiamond particle, Figure 1, exhibits electrostatic effects at the material interfaces and a strong nonlinear variation of the field near these interfaces. The surface electric field of the composite needle in the region of the nanodiamond cluster exhibits a strong field enhancement ( $\gamma$ ) at the MIV triple junction, weak enhancement at the insulator vacuum interface, and field reduction, indicated by  $\gamma < 1$ , at the metal insulator back contact, Figure 2. These size and shape selective electrostatic field reduction and enhancement effects modify the emission area and current through the introduction of electron trajectory dependent processes. The electron trajectory dependent processes involve the transport of electrons tunneling from the MIV triple junction through

the diamond nanodot and an effective potential barrier near the MIV triple junction induced by the interaction between the metal and nanodiamond surface potential barriers<sup>11</sup>.

The electrostatic potential and field distributions of the three structures exhibiting thickness dependent field emission current-voltage characteristics were analyzed for the relative effects of cathode geometry and material on the field emission process. The electrostatic field enhancement at various interfaces of the three structures as a function of the relative permittivity and size of the particle are shown in Figure 3 and Figure 4 respectively. Figure 3a indicates that the maximum electrostatic field for a low permittivity coatings,  $\epsilon < 3$ , occurs at the metal-coating interface, but for coatings with  $\epsilon > 3$ , such as diamond, that the field is a maximum at the coating-vacuum interface. Figure 3b indicates that that the maximum electrostatic field for the conformal particle model transitions from the metal-diamond interface to the diamond-vacuum interface at  $\epsilon \approx 2$ . Field enhancement at the triple junction and the apex of the particle decreases similarly as the size of the particle is increased, Figure 4a, however field enhancement at the apex decreases and increases at the triple junction as the particle size is increased, Figure 4b. Field enhancement at the triple junction is dominated by material effects in the case of the conformal particle, however for the embedded particle geometric field enhancement dominates at the triple junction as demonstrated by the field enhancement increase as the size of the particle is increased as seen in Figure 6b.

The potential barrier for the conformal and semi-embedded particle as a function of relative permittivity and particle size are shown in Figure 5 and 6 respectively. The potential barrier in and near the conformal particle varies nearly linearly as both a function of relative permittivity and particle radius. In and near the semi-embedded particle the

potential barrier varies nonlinearly creating a hump in the potential near the diamond metal interface that varies with the permittivity and size of the particle. This potential barrier hump corresponds to the local decrease in the field near the diamond metal interface seen in Figure 1 and 2. The accuracy of conventional triangular barrier Fowler Nordheim analysis when applied to semi-embedded particles will depend on the strength of this nonlinearity and may require a new model of the cold field emission process that accounts for this nonlinear potential variation.

### 3.6. Conclusions

The electrostatic properties of metal-insulator composite needles were analyzed numerically for effects of particle size, shape, and relationships to the underlying metal substrate needle. HRTEM and EELS analysis of composite needles consisting of discrete diamond nanoparticles deposited on Mo needles indicate that the composition of the nanoparticles is dominated by carbon in the diamond phase and geometrically the particles are embedded in the Mo needle. It was found that MIV triple junction and particle morphology effects can have a significant influence on the near surface potential barrier and resultant field emission behavior of such needle structures. Our results indicate that classical electrostatic and Fowler-Nordheim analysis cannot wholly explain the thickness and size selective dependencies of diamond nanodot coated Mo field emission experiments. Understanding these “anomalous” effects requires further inquiry into the structure of the near surface potential barrier, quantum confinement effects and surface phenomena that may effect electron emission.

### 3.7. Acknowledgements

The authors would like to thank T. Tyler and A. Kvit for discussions of the HRTEM and EELS data cited in this manuscript<sup>9</sup>. This work was supported through by the Semiconductor Research Corporation and the Department of Energy.

### 3.8. References

- <sup>1</sup> V.V. Zhirnov, C. Lizzul-Rinne, G.J. Wojak, R.C. Sanwald, J.J. Cuomo, J.J. Hren, *J. Vac. Sci. Technol. B*, **19**, 17, (2001).
- <sup>2</sup> D. Kang, V.V. Zhirnov, R.C. Sanwald, J.J. Hren, J.J. Cuomo, *J. Vac. Sci. Technol. B*, **19**, 50, (2001).
- <sup>3</sup> M.W. Geis, N.N. Efremow, K.E. Krohn, J.C. Twichell, T.M. Lyszczarz, R. Kalish, J.A. Greer, M.D. Tabat, *Nature*, **393**, 431, (1998).
- <sup>4</sup> R.G. Forbes, *Solid State Elect.*, **45**, 779, (2001).
- <sup>5</sup> V.V. Zhirnov, W.B. Choi, J.J. Cuomo, J.J. Hren, *App. Surf. Sci.*, **94-95**, 123, (1996).
- <sup>6</sup> A.F. Belyanin, L.L. Bouilov, V.V. Zhirnov, A.I. Kamenev, K.A. Kovalskij, B.V. Spitsyn, *Diamond and Related Materials*, **8**, 369, (1999).
- <sup>7</sup> A.F. Belyanin, P.V. Pashchenko, B.V. Spitsyn, A.N. Blaut-Bachev, L.L. Bouilov, V.V. Zhirnov, L.V. Bormatova, E.I. Givargizov, *Diamond and Related Materials*, **7**, 692, (1998).
- <sup>8</sup> V. V. Zhirnov, A. N. Alimova, J. J. Hren, *Applied Surface Science*, **191**, 20, (2002).
- <sup>9</sup> T. Tyler, V. V. Zhirnov, A. V. Kvit, D. Kang and J. J. Hren, *Appl. Phys. Letts.*, **82**, 2904, (2003).
- <sup>10</sup> D.L. Jaeger, J.J. Hren, V.V. Zhirnov, *J. Appl. Phys.*, **93**, 691, (2003).

- <sup>11</sup> J.B. Cui, J. Ristein, L. Ley, Phys. Rev. B, **60**, 16135, (1999).

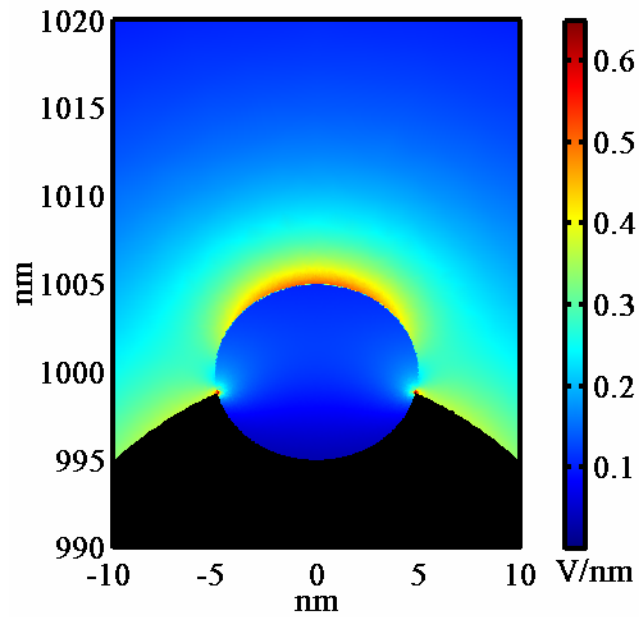


Figure 1. Field distribution near the apex of a metal insulator composite needle exhibits behavior strongly dissimilar to that experienced by a wholly metal composite needle; particle radius is 5nm  $\epsilon_r = 5.7$  and an applied bias of 1000V.

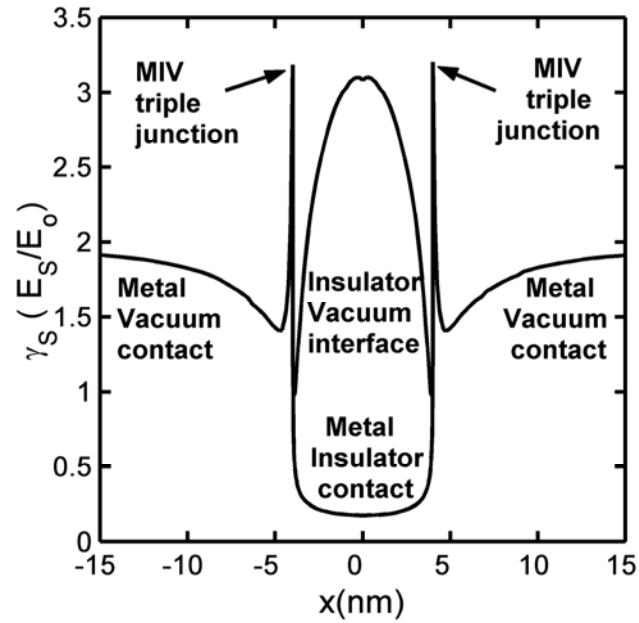
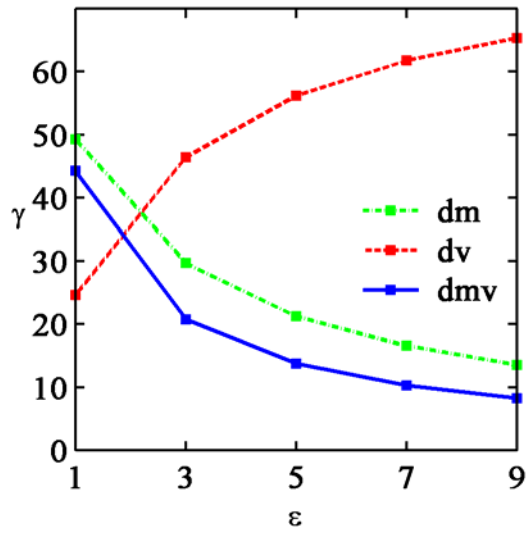
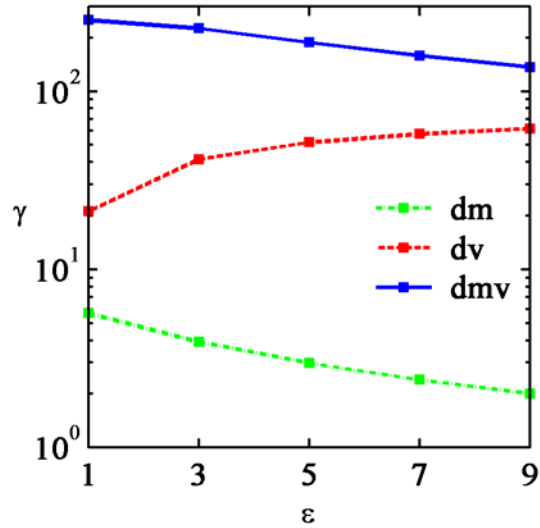


Figure 2. Extracted field enhancement values along the metal-diamond (MD), metal-vacuum (MV), diamond-vacuum (DV) and metal-diamond-vacuum (MDV) interface surfaces for the embedded nanodiamond particle model system with particle radii of  $r=5\text{nm}$  and relative permittivity of  $\epsilon_r = 5.7$ .

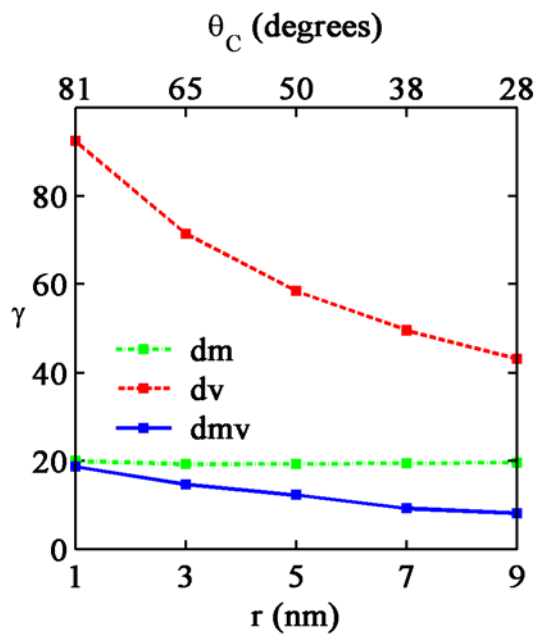


(a)

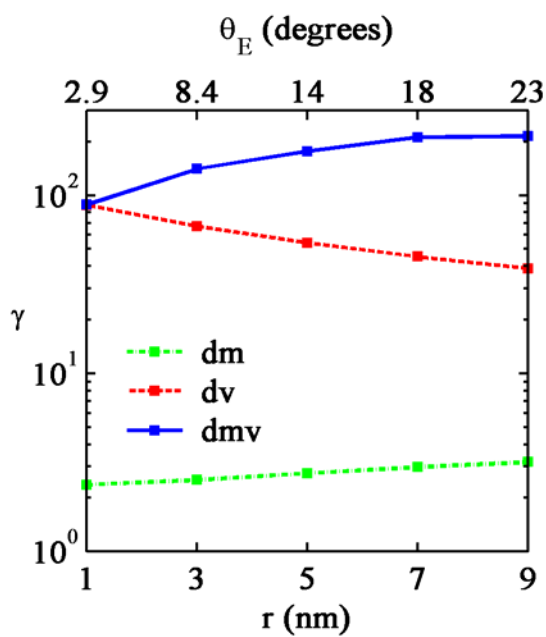


(b)

Figure 3. Electrostatic field enhancement at several points of interest,  $dm$  – metal diamond interface,  $dv$  – diamond vacuum interface and  $dmv$  – metal diamond vacuum interface, as a result of varying the dielectric permittivity of the particle for a a) conformal particle and b) semi-embedded particle of radius 5nm.

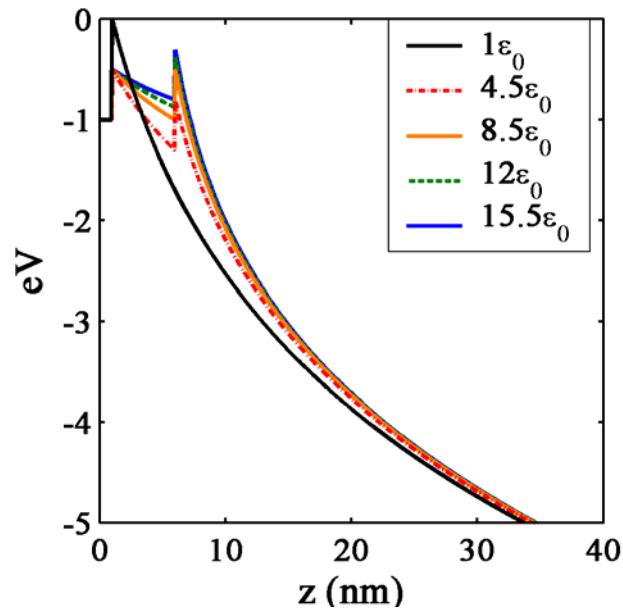


(a)

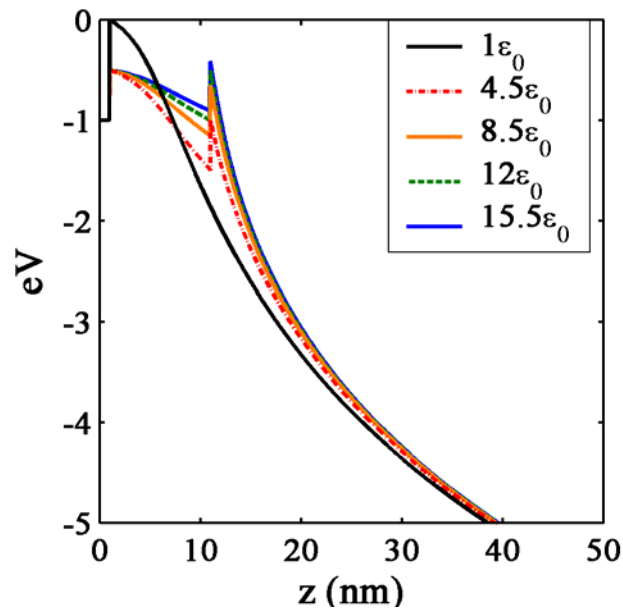


(b)

Figure 4. Electrostatic field enhancement at several points of interest, dm – metal diamond interface, dv – diamond vacuum interface and dmv – metal diamond vacuum interface, as a result of varying the particle radius for a) conformal particle and b) semi-embedded particle of relative dielectric permittivity 5.7.

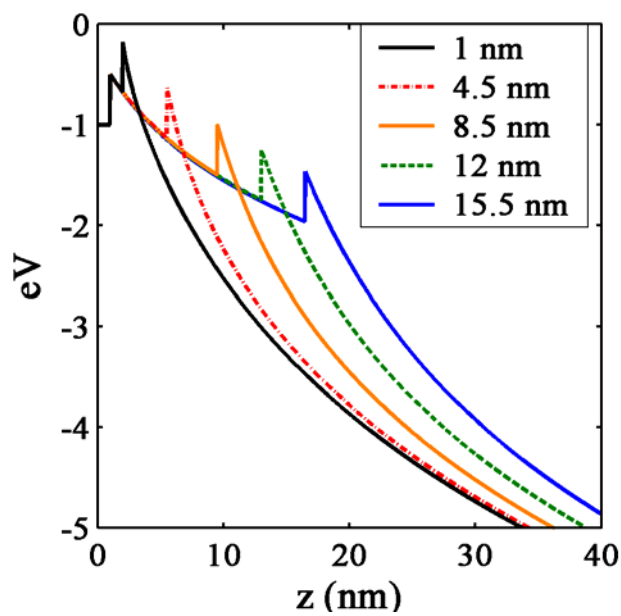


(a)

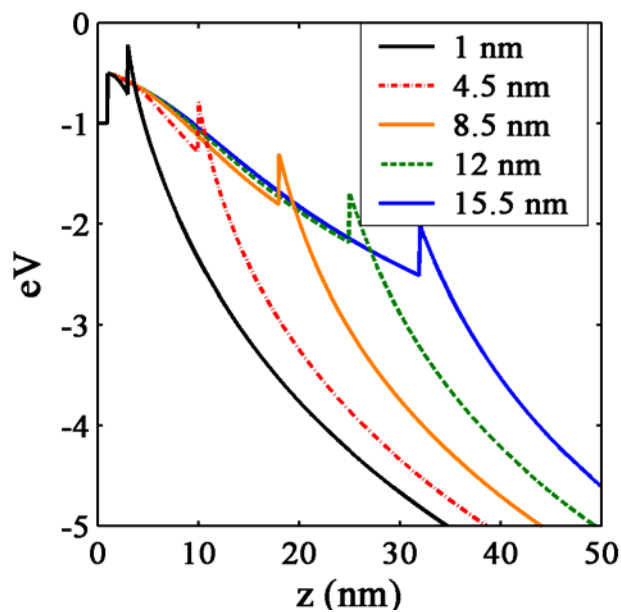


(b)

Figure 5. Electrostatic conduction band potential normal to the center of revolution of a composite needle for a) a conformal particle and b) a semi-embedded particle of radius 5nm and an applied bias of 1000V.



(a)



(b)

Figure 6. Electrostatic conduction band potential normal to the center of revolution of a composite needle as a function of particle radius for a) conformal particle and b) semi-embedded particle of relative dielectric permittivity 5.7 and an applied bias of 1000V.

## **Chapter 4. Field Emission Device with Back-Gated Structure**

by

V. P. Mammana, D. Jaeger, O. Shenderova, G. E. McGuire

International Technology Center, P.O. Box 13740

Research Triangle Park, NC 27709

published in

Journal of Vacuum Science and Technology (2004)

#### 4.1. Abstract

Analysis and performance optimization of a back-gated field emission device (FED) is provided. The device consists of an anode, electron emitting cathodes and gate electrode that is placed below the cathode (“back-gate”). The role of a back-gate is to control electron emission from the cathode by changing the voltage on the back gate. The top of the cathode is selectively coated with an electron emissive material/structure that presents better emission properties when compared to the material of the cathode. The role of the cathode geometry, back gate voltage, cathode-gate distance, distance between cathode electrodes, the back gate dielectric, as well as field emission characteristics of the emitting material on the top of a cathode were analyzed using continuum electrostatic simulations. The proposed design significantly facilitates fabrication of the field emitting devices while decreasing the amount of charge lost to the gate and potentially reducing the likelihood of catastrophic discharges.

#### 4.2. Introduction

Recently, a new class of triode structures for field emitting devices had been suggested, 1-3 the so called under-gate type triode field emitters where the gate electrodes are located underneath the cathode electrodes. The structure consists of three parallel flat conductors juxtaposed in the following order: anode, cathode and gate. The cathode and anode electrodes are separated by a vacuum gap while the gate electrode is separated by an insulating layer from the cathode electrode. The cathode electrode is smaller in size than the other two, so that the insulating layer is exposed in selected areas. As a result, a subset of field lines starting at the gate surface go around the cathode borders at exposed portions of the dielectric, influencing the field emission from the opposite side of the cathode surface

(side facing away from gate or simply “top”). This influence is maximized by the incorporation of carbon nanotubes (CNTs) into the top of the cathode,<sup>1-3</sup> so that emission occurs at an operating voltage that is sufficient to produce emission from the nanotubes but is too small to produce emission from the other parts of the cathode, even if those are closer to the gate. In such a configuration, by the appropriate selection of electrode distances and anode voltage, one can effectively control the emission from the cathode top by modulating the gate voltage in a range much smaller than the anode voltage.

The design proposed by Y.S. Choi et al. and S.G. Yu et al. <sup>1-3</sup> significantly facilitates fabrication of the FED because it avoids dielectric patterning that is typical for conventional triode structures and relies solely on thin film deposition and metal patterning. In a conventional gated FED (gated tip arrays) the dielectric layer and gate layer surrounding tips are patterned increasing the number of process steps required and ultimately the cost of fabricating the device.

In an under-gate type emitter as proposed by Y.S. Choi,<sup>3</sup> the field at the edges of the cathode plane is intensified and this region generates the majority of electrons emitted. This results in a relatively high dispersion of the emitted electron beam<sup>3</sup> while the entire surface of a cathode can not be effectively used for electron emission due to field screening at the center of the electrode. In addition, as reported by Choi, a certain fraction of electrons is directed toward the gate causing dielectric charging<sup>3</sup> although the majority of the electrons are indeed attracted toward the anode. This charging screens the gate field and may also result in catastrophic discharges. Ways to address this problem include the use of a discharging cycle, thus consuming extra power, or the patterning of the dielectric layer, thus increasing the processing steps and exposing the gate metal.<sup>3</sup> The overall device robustness is reduced,

since most of the catastrophic events in a FED are related to discharges between electrodes.<sup>4</sup> In addition, it decreases the power efficiency, since the parasitic gate current increases due to the removal of the dielectric protection.

In a similar way, a horizontal edge emitter was proposed by Johnston et al.,<sup>5</sup> where the edge cathode emits electrons horizontally, which are deflected toward the anode by a negatively biased electrode that is substantially in the same plane as the cathode. For instance, a combination of the approaches proposed by Y.S. Choi<sup>1-3</sup> and Johnston et al.<sup>5</sup> could be another alternative to better address the drawbacks of backward emission, having as a penalty the increased complexity.

In the current paper, we propose a new configuration for back-gated devices with the potential to achieve significantly improved performance, as indicated by theoretical calculations. In this configuration the fraction of electrons emitted toward gate is reduced by the careful selection of the cathode geometry, so that deflecting electrodes are not required.

In the proposed configuration a cathode cross-section is chosen in a way to reduce the electrostatic field screening at the center portions of the top of the cathode. This geometry, combined with the integration of a layer of low apparent work function material, such as carbon nanotubes (CNTs) at the top surface of the cathode, restricts the emission within a reduced area around the crest of the cathode emitter. Electrons emitted from the crest are more likely to be directed toward the anode, instead of being accelerated back to the gate. Note that we use the term apparent work function to identify the slope of a  $\ln(I/E^2) \times (1/E)$  plot (Fowler-Nordheim plot), in which  $E$  is the macroscopic field calculated by  $E=V/d$  for a parallel diode-type field emission experiment.

The mentioned low apparent work function material will be referred here as *emissive material/structure* (EMS), as an indication that the functionality of the device does not depend on the particular material selected, as long as one is capable of selectively constraining the emission within the crest of the cathode.

In the next sections we describe a first approach for the optimization of the overall performance of the device in terms of the cathode geometry, parasitic capacitance, transconductance, back gate voltage, cathode-gate distance, distance between cathode electrodes (the cathodes are a set of uniformly spaced parallel stripes), dielectric constant of the back gate insulator, as well as field emission properties of the EMS so that we try to predict what is the highest possible current one can achieve from a back-gated triode. This optimization is carried out in a microwave application context; however the proposed concept can be extended to display applications with minor changes specific for pixel addressing.

### 4.3. Experiments

#### 4.3.1. Fabrication of the back-gated device structure

There are several alternatives for the fabrication of a structure in the general form of the idealized device described above and shown in Fig. 1. For instance, the process can be started by SiO<sub>2</sub> layer formation by thermal oxidation. Subsequently, a thick layer of resist can be patterned over the SiO<sub>2</sub> in order to form opened stripes where the SiO<sub>2</sub> is exposed. By evaporating a metal layer over the patterned resist it is possible to form metal lines along the exposed stripes. After lift-off the resist, the back-gate structure is formed, where the Si substrate serves as the gate and the metal stripes perform as the cathodes. The anode is a flat

and conductive plane that is positioned above and parallel to the Si plane. Using one of several candidate deposition techniques such as chemical vapor deposition (CVD) or paste printing, the crest of the cathode stripes can be selectively coated with a low effective work function material such as CNTs, for example. This sequence of processing steps leads to a device with a cathode geometry that is substantially prismatic in shape, with a trapezoidal cross section.

As mentioned in the introduction section of this paper, rounding off the cathode edges intends to reduce the field screening at the central portions of the top surface of a cathode. Although a cylindrical cathode structure as shown in Fig. 1 is difficult to produce microscopically, rounding the top edges of a trapezoid can be accomplished by different means, for example, by sputtering.

#### **4.3.2. Cathode-Gate Model: Cylinder-Plane geometry**

In this subsection, the field profiles for a cathode presenting a cylindrical geometry and a rectangular profile are compared, where an aspect ratio for the rectangular profile is different from one (a width is larger than height). The analysis includes an estimate of the field strength above the cathode surface at a given gate voltage, which is adequate for producing electron emission from the EMS placed at the top of the cathode.

In general, it follows from the solution of the Laplace equation that the field at the surface of a conductive cylinder in the cylinder-over-plane geometry depends on the potential applied to the conductive gate.<sup>6</sup> The field at the side of the cathode that is closer to the plane (in contact with the dielectric) is higher than the field over the crest, which is the side that is far from the plane. However, the magnitude of the lower field above the cylinder still

depends on the plane potential. Figure 2a illustrates the field above the surface of a cylinder along its perimeter, as a function of angular coordinate. The numerical calculation had been carried out for a cylinder placed between two conducting biased planes representing a back-gate and an anode. For the condition of zero gate voltage, the anode voltage is selected to produce a field below  $1 \text{ V}/\mu\text{m}$ , which we assume is insufficient for inducing emission from any EMS present at the top of the cathode. When bias in the range of 20 - 30 V is applied at the gate ('on' status), the field above the cathode ( $\sim 10 \text{ V}/\mu\text{m}$ ) is sufficient to produce electron emission from an EMS containing CNTs, for example, while other types of EMS may require different voltage ratios. At the 'on' status conditions described above, the field below the cathode is higher than at the top of the cathode, but not high enough to initiate field emission from the cathode metal toward the gate (we assume that a typical macroscopic field required for field emission from metal surfaces is within the range of 25 - 30  $\text{V}/\mu\text{m}$ ). As it follows from Fig. 2a, the field above the cathode is approximately the same for angular coordinate  $\Theta$  up to 30 degrees, so that in the ideal case uniform emission from an EMS material deposited within the area restricted by  $\Theta < 30^\circ$  can be expected. For a real EMS such as CNTs, the emission will be concentrated at the tallest nanotubes or highest field points. The field required for electron emission from different parts of the cathode can be also analyzed in terms of an apparent work function. In order to guarantee field emission from the top of the cathode, the apparent work function of the EMS material present at the cathode crest has to be essentially lower than that of the cathode. The width of the EMS line deposited at the cathode crest is determined by the requirement that the electron trajectories for every electron generated at the EMS travels toward the anode. The trajectory simulations that were carried out will not be described in this paper.

The field strength above the surface of an under-gated geometry as suggested by Y.S. Choi and S.G. Yu<sup>1-3</sup> is presented in Fig. 2b. The cross-section of the cathode has a rectangular shape with 1:1 and 1:2 aspect ratios and a geometrical size similar to that for the circle in the cylindrical geometry. The two peaks in the curve illustrated in Fig. 2b correspond to the field above rectangle edges. As can be concluded from the comparison with Fig. 2a, the field at the crest of the cathode generated in the stripe geometry is approximately half of that generated for a cylindrical cathode at similar geometrical/voltage parameters, while the former presents a maximum field close to the cathode edge that is higher than the maximum field presented by the later.

### 4.3.3. Simulation Setup

The back-gate structure based on a cylinder plane geometry schematically illustrated in Fig. 3 was modeled as a field emitting source of electrons with the total effective device area of  $W_{Device}^2$ . Copper wires had been modeled assuming the following ideal conditions: absence of surface roughness and absence of an oxide layer or surface adsorbates. Geometrical and material parameters of the simulated wires are provided in Table 1. Two cathode shapes were simulated: (i) a half-cylindrical and (ii) a trapezoidal profile; which are profiles that are close to the one practically achievable by the method proposed in the fabrication section.

The EMS structure simulated consisted of arrays of capped single wall carbon nanotubes, (SWCNT), aligned perpendicular to and along the center of the metal cathode lines, as shown in the inset of Fig. 3. The distance  $w_{SWCNT}$  between nearest SWCNT was optimized to avoid mutual screening of CNTs and therefore maximize the total Fowler-

Nordheim tunneling current. According to the geometrical and material parameters for SWCNT indicated in Table 1, the geometric field enhancement factor  $\gamma_{SWCNT}$  was determined after the mentioned optimization of the SWCNT field emission current. The back gate dielectric layer was modeled as an ideal dielectric with the relative permittivity  $\epsilon_{BGD}$  without interface or surface traps present.

Calculation of the emitted current and capacitance of the back gate structure required knowledge of the electrostatic fields and potentials. The related Laplace's equation with boundary conditions corresponding to the back gate structure, illustrated in Fig. 3, was solved by the application of the finite element method with adaptively sized second order Lagrange elements using the FEMLAB package.<sup>7</sup> Laplace's equation was analyzed on two three-dimensional geometric domains. First we used a cylindrically symmetric "needle-on-plane" geometry to represent a single SWCNT sticking out from the surface, followed by a plane symmetric formulation representing the general back gate structure geometry without the EMS. In order to use a 2D computational space, we explored the specific symmetries of the problem, as in D.L. Jaeger et al.<sup>8</sup> We calculated the capacitance of the back gate structure with respect to the gate bias using the total electric energy method.<sup>6</sup>

The electrostatic field perturbed by the presence of a single SWCNT, relative to the electrostatic field of the uncoated cathode back-gate structure,  $E_0(\mathbf{r})$ , was modeled using the two stage field enhancement model.<sup>8</sup> Using the two stage field enhancement model the electrostatic field along the surface of the back-gate structure is

$$E(\mathbf{r}) = \begin{cases} \gamma_{SWCNT} E_0(\mathbf{r}) & \text{if } \mathbf{r} \in \Omega_{SWCNT} \\ E_0(\mathbf{r}) & \text{otherwise} \end{cases} \quad (1)$$

where  $\Omega_{SWCNT}$  is the space occupied by the SWCNT cathodes..

The emitted current density from the surface of a single SWCNT cathode,

$$J_{FN}^{SWCNT}(\mathbf{r}) \approx \frac{1.54(\gamma_{SWCNT} E_0(\mathbf{r}))^2}{\phi_{SWCNT}} \exp\left(-\left(\frac{6.83\phi_{SWCNT}^{1.5}}{\gamma_{SWCNT} E_0(\mathbf{r})}\right)\right) \quad (2)$$

was derived from the conventional Fowler-Nordheim equation.. One can express the integrated current for the back gate device under the condition that emission is dominated by the SWCNT coating by

$$I_{Device} \approx I_{Device}^{SWCNT} = \int_{\Omega_{Device}} J_{FN}(\mathbf{r}) d\mathbf{r} = n_{wire}^{Device} I_{wire}^{SWCNT} \quad (3)$$

in such a way that the number of SWCNT coated wires is  $n_{wire}^{Device} = \frac{W_{Device}}{2w_{wire}}$ . The integrated

current per wire due to the total number of SWCNT per wire,  $n_{SWCNT}^{wire} = \frac{L_{wire}}{2w_{SWCNT}}$ , is

$$I_{wire}^{SWCNT} = \int_{\Omega_{wire}} J_{FN}(\mathbf{r}) d\mathbf{r} = n_{SWCNT}^{wire} I_{SWCNT} \quad (4)$$

and the emission current due to a single SWCNT with an emission area  $A_{emission}^{SWCNT} \approx \Delta x_{SWCNT}^2$  is

$$I_{SWCNT} = \int_{\Omega_{SWCNT}} J_{FN}(\mathbf{r}) d\mathbf{r} = A_{emission}^{SWCNT} J_{FN}^{SWCNT}(\mathbf{r}) \quad (5)$$

Morphological or material differences between the individual SWCNT that would affect the field emission process were modeled as the proportion of sites per cathode wire that emit electrons,  $\kappa$ . Using the physical parameters from Table I and the previous limits and formulae for the field emitted current the total device current for the back-gate structure with SWCNT coated cathode wires is

$$I_{Device} \approx \frac{1}{4} \frac{\kappa W_{Device} L_{wire} \Delta x_{SWCNT}^2}{w_{wire} w_{SWCNT}} J_{FN}^{SWCNT}(\mathbf{r}) \quad (6)$$

The transconductance,  $g = \frac{\partial I_{Device}}{\partial \Phi}$ , was determined as a function of the back-gate electrode potential  $\Phi_{gate}$  using a 2<sup>nd</sup> order centered difference equation.

#### 4.4. Results and Discussion

Figure 4 indicates the effect of shielding on the electrostatic field, current and capacitance due to neighbor cathode interactions. We observed that the cathode stripes separation significantly affect the electrostatic and emission characteristics of the device, as shown in Fig. 4a. The field at the SWCNT apex that experiences shielding from neighboring cathodes closer than 10  $\mu\text{m}$  is significantly smaller than the unshielded field experienced by a similar isolated SWCNT structure. The calculated maximum emitted current from the SWCNT is observed to occur when the cathode pitch is in the range 7-9  $\mu\text{m}$ . In a parallel cathode configuration as proposed here, the total emitted current increases proportionately to the number of emitting cathode stripes, but in the context of the concurrent effect of a reduction of the current because of the field screening due to a closer-packing of the metal lines. This situation leads to a device that has its optimal performance strongly dependent on the cathode line to cathode line spacing.

The capacitance of the back gate structure is also strongly affected by the cathode line separation, as shown in Fig. 4b, decreasing approximately an order of magnitude in the interval 2 to 20  $\mu\text{m}$ . Special attention should be dedicated to the capacitance while optimizing the back-gate structure, especially if the application under consideration is microwave tube electron sources, wherein higher capacitances limit switching speeds due to capacitive charging/discharging times. From the approximately inverse power law behavior of the capacitance as a function of the cathode separation, where overall

slope  $\frac{dC}{dw} \approx -1.0 \times 10^{-9} F/\mu m$ , it is observed that tightly packed arrays of cathode lines have the disadvantage of much higher capacitance. Therefore, optimization of the back gate structure as a function of the cathode line separation should consider the conflicting interests of maximizing the emitted current and of minimizing the device capacitance. Analysis of Fig. 4a and Fig. 4b indicates that in the separation range of 7 – 9  $\mu m$ , where  $\frac{dC}{dw} \approx -1.7 \times 10^{-10} F/\mu m$ , we can maximize the current and lower the capacitance in comparison to the 2-5 $\mu m$  regime, where  $\frac{dC}{dw} \approx -2.4 \times 10^{-8} F/\mu m$ .

Figure 5 indicates that the back gate voltage,  $\Phi_{gate}$ , effectively controls the emission current and determines the effective optimum cathode spacing. A 50 V change in  $\Phi_{gate}$  gives almost an order of magnitude change in the emission current,  $I_{Device}$ . From Fig. 5 we conclude that the optimum cathode spacing increases with increasing  $\Phi_{gate}$ , indicating that the EMS field is a function of both  $\Phi_{gate}$  and  $w_{wire}$ . The variation of the optimum cathode spacing with respect to  $\Phi_{gate}$  is assumed to be smooth and the step-like behavior shown in Fig. 5 is due to a relatively coarse discretization of the cathode spacing. Fig. 4a shows that  $I_{Device}$  peak shifts to larger  $w_{wire}$  with increasing  $\Phi_{gate}$ , and consequently, following Fig. 4b, the capacitance decreases. The optimum  $w_{wire}$  can be determined by the optimum device voltage that (at the same time) guarantees high-frequency device operation and sufficiently large device currents, within acceptable power regimes, when  $\Phi_{gate}$  is set to the ‘on’ status.

Figure 6 indicates how the dielectric layer affects the emission characteristics. Figure 6a indicates that the device emission current and SWCNT apex field are enhanced by the back gate dielectric permittivity in the regime of  $\epsilon_{BGD} < 10$ . This regime of dielectric

permittivities includes many materials, such as  $\text{SiO}_2$ , which can be easily incorporated into the device fabrication process and provides for a reduction in the capacitance if the back gate dielectric is modeled as a parallel plate dielectric capacitor. In Fig. 6b, the device emission current and SWCNT apex field is enhanced by approximately a factor of 3 by reducing the dielectric thickness. This general trend towards smaller back gate dielectric thicknesses will have to be balanced against the capacitance of the structure, which will increase as the dielectric thickness decreases.

The device emission current and transconductance characteristics of two representative cathode substrate structures, a half cylinder and a trapezoid, were determined relative to the back gate electrode potential  $\Phi_{\text{gate}}$  in Fig. 7. The device current and transconductance characteristics of the half cylinder cathode (Fig. 7b) is approximately a factor 3 better than similar device current and transconductance characteristics calculated for a trapezoidal cathode (Fig. 7a). Analysis of the cathode current and transconductance characteristics of Fig. 7a and Fig. 7b indicates that a high aspect ratio cathode wire is an efficient substrate geometry for the SWCNT EMS array coating considered during the simulation, as illustrated in the inset of Fig. 3.

#### 4.5. Conclusions

The preliminary optimization presented in this paper for a back gate structure for microwave applications indicated that  $w_{\text{wire}}$ , cathode shape,  $\epsilon_{\text{BGD}}$  and  $h_{\text{BGD}}$  have important consequences on the device characteristics, primarily the emitted current and capacitance. An interesting aspect of the current work is the fact that the considered geometry of regular arrays of emission sites located along the center of the metal cathode wires may provide a

fairly uniform/laminar beam due to the periodicity of emission sites and confinement of electron emission to a narrow cathode surface angle. This preliminary optimization showed that theoretically, for an ideal cathode with 100% of the CNTs emitting, we can approach a total current density for the device approximately  $100 \text{ A/cm}^2$ . The authors are currently working on the simulation of the electrons trajectories.

#### **4.6. Acknowledgements**

The authors would like to acknowledge support from the Office of Naval Research, award N00014-02-1-0711.

#### 4.7. References

- <sup>1</sup> Y.S.Choi, J.H. Kang, Y.J Park et al., *Diam. Rel. Mat.* **10**, 1705 (2001)
- <sup>2</sup> S.G Yu, W.K.Yi, J.Lee, T.Jeong, S.H.Jin, J.Heo, J.H. Kang, Y.S.Choi, C.S. Lee, J.B.Yoo, J.M. Kim *Appl.Phys.Let.* **80**, 4036 (2002)
- <sup>3</sup> Y.S. Choi, J.H. Kang, H.Y. Kim, B.G. Lee. et al., *Appl. Surf. Sci.*, in press
- <sup>4</sup> I. Brodie and C.A. Spindt, “Vacuum microelectronics”, *Adv. in Electronics and Electron Physics*, **83**,1 (1992)
- <sup>5</sup> B.R. Johnson, A.I. Akinwande, D. Murphy, *J. Vac. Science and Technol. B* **15**, 535 (1997)
- <sup>6</sup> Reitz-Milford Foundations of electromagnetic theory / John R. Reitz, Frederic J. Milford, Robert W. Christy. 1993
- <sup>7</sup> FEMLAB software of COMSOL, Inc., Burlington, MA 01803, USA
- <sup>8</sup> Jaeger DL, Hren JJ, Zhirnov VV, *J. Appl. Phys.* **93**, 691 (2003).

Table I. Physical parameters used in the Fowler-Nordheim current analysis.

Parameter	Meaning/Equation	Value
$W_{Device}$	Device width (mm)	1
$r_{wire}$	Wire base radius ( $\mu\text{m}$ )	0.47
$\phi_{wire}$	Wire work function (eV)	5.15
$\gamma_{wire}$	Wire field enhancement	1
$L_{wire}$	Wire length (mm)	1
$w_{wire}$	$\frac{1}{2}$ inter-cathode wire separation ( $\mu\text{m}$ )	variable
$r_{SWCNT}$	SWCNT radius (nm)	3
$h_{SWCNT}$	SWCNT height ( $\mu\text{m}$ )	3
$\phi_{SWCNT}$	SWCNT Work function (eV)	4
$\gamma_{SWCNT}$	SWCNT single tube field enhancement	530
$w_{SWCNT}$	$\frac{1}{2}$ inter-SWCNT separation ( $\mu\text{m}$ )	2
$\Delta x_{SWCNT}$	SWCNT effective width of emission (nm)	1
$\epsilon_{BGD}$	Back gate dielectric relative permittivity	variable
$h_{BGD}$	Back gate dielectric thickness ( $\mu\text{m}$ )	variable
$\Phi_{gate}$	Back gate electrode potential (V)	variable
$\kappa$	proportion of emitting SWCNT sites per wire	$1 \div 100$

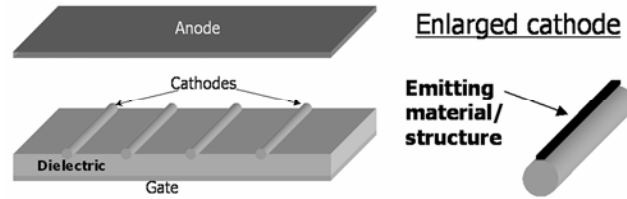
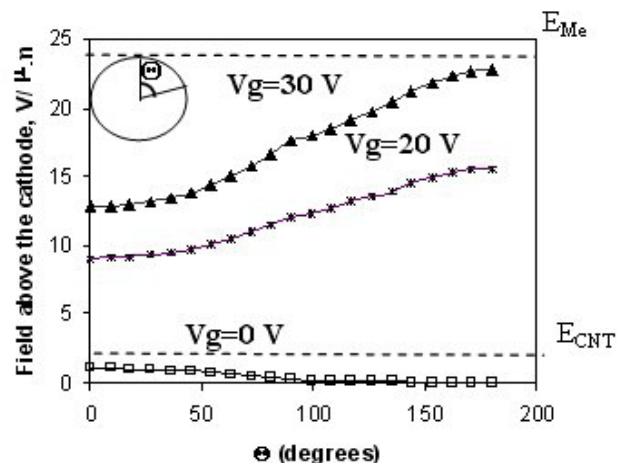
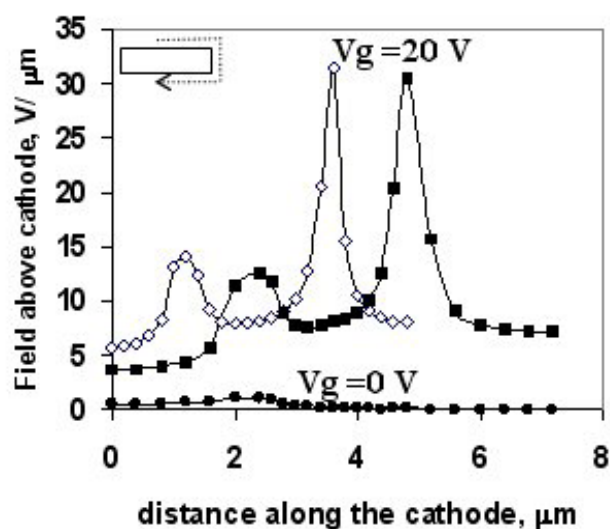


Figure 1. Schematic representation of the back gated device with cathodes implemented as wire arrays (left). Enlarged view of the cathode (right), containing field emitting material (low work function material or carbon nanotube/polymer composite, for example) at the top. Other EMS alternatives could be used, such as tips fabricated at the top of the cathode.



(a)



(b)

Figure 2. Field above the cathode for cylindrical cathode (a) and a cathode rectangular in its cross section (b). Cathodes profiles are shown in the left up corners. Field is shown as a function of the angular coordinate (a) and as a function of length along the rectangle perimeter (b). Anode voltage is 500V, cathode-anode distance is 1 mm, cathode-gate distance is 3  $\mu\text{m}$ , dielectric constant of the insulator layer equals 4. Diameter of a cylindrical cathode is 2  $\mu\text{m}$  (a), sizes of rectangles in a cross section of cathode (b) are 2x2 $\mu\text{m}^2$  ( $\diamond$ ) and 2x4  $\mu\text{m}^2$  ( $\blacksquare$ ). Dashed horizontal lines in (a) correspond to typical macroscopic fields required to initiate field emission from material containing carbon nanotube ( $E_{CNT}$ ) and from metallic flat surface ( $E_{Me}$ ).

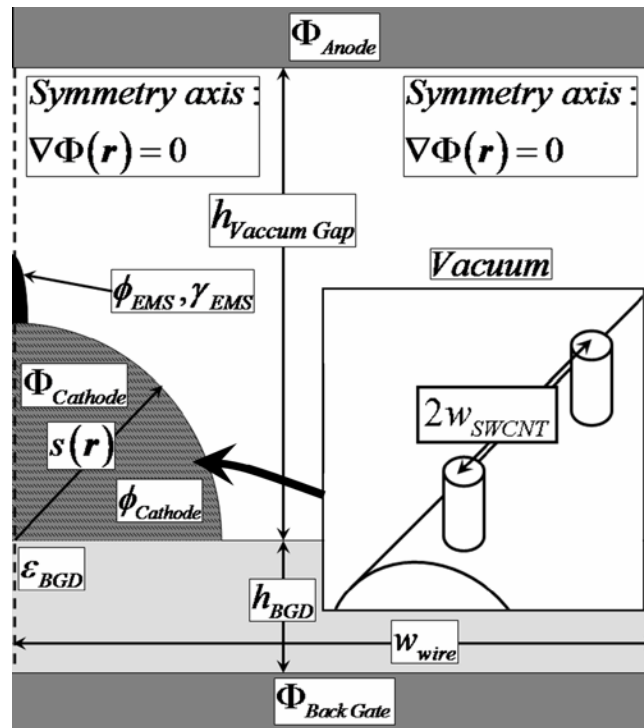
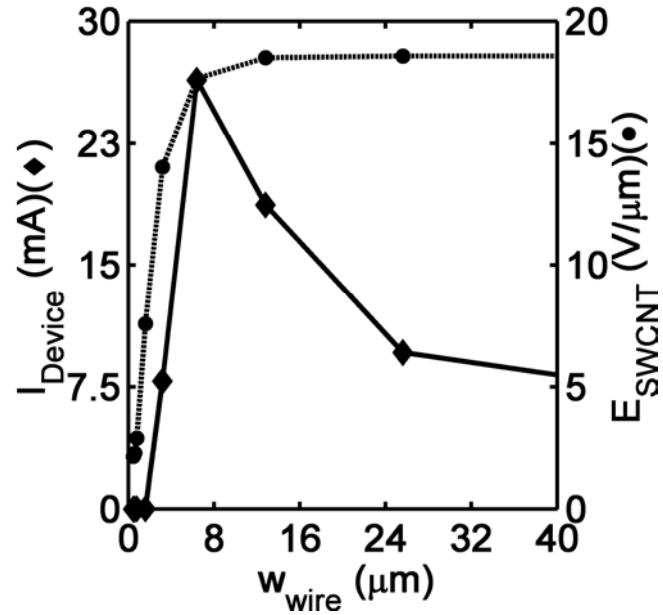
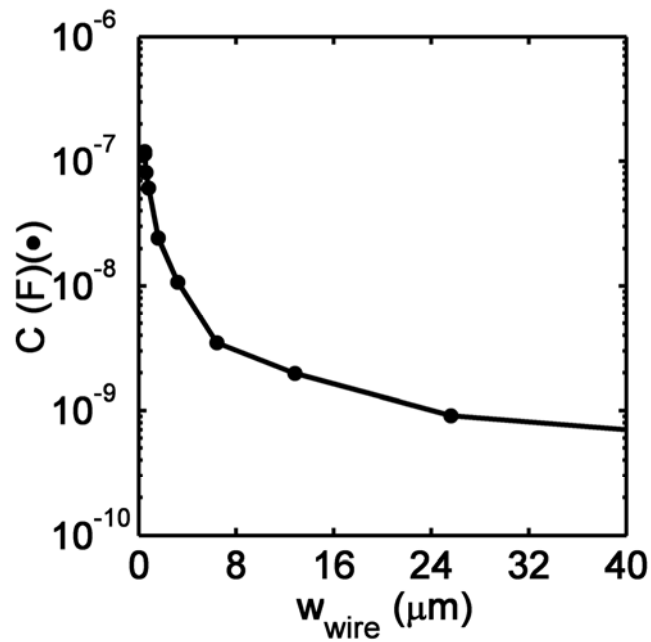


Figure 3. Schematic general model of the back gate structure and SWCNT arrays on a cathode substrate wire with relevant material and boundary condition parameters indicated. (acronyms BGD and EMS stand for back gate dielectric and emissive material/structure, respectively).



(a)



(b)

Figure 4. Variation of the emission and electrostatic properties for the optimized SWCNT EMS structure, a) integrated current  $I_{\text{Device}}$  and maximum electrostatic field at the EMS surface  $E_{\text{SWCNT}}$ , b) capacitance of the back gate structure  $C$ , as a function of the separation between the gate metal cathode lines  $w_{\text{wire}}$ . Relevant parameters used:  $\Phi_{\text{Gate}} = 30\text{V}$ ,  $\Phi_{\text{Anode}} = 200\text{V}$ ,  $h_{\text{BGD}} = 3.1\mu\text{m}$ ,  $h_{\text{gap}} = 20\mu\text{m}$ ,  $\gamma_{\text{SWCNT}} = 500$ ,  $\epsilon_{\text{BGD}} = 4$ .

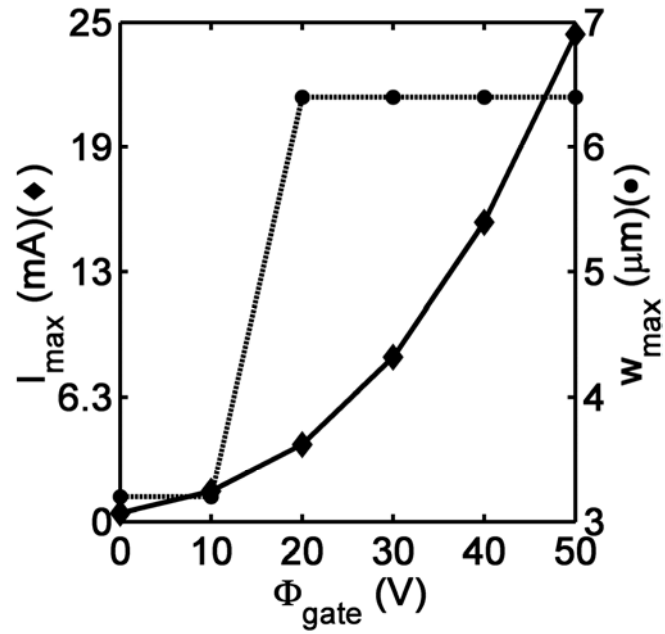
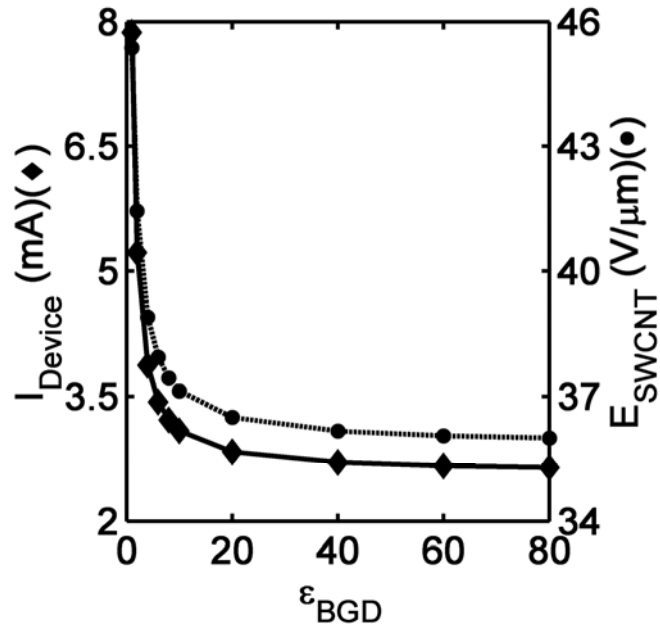
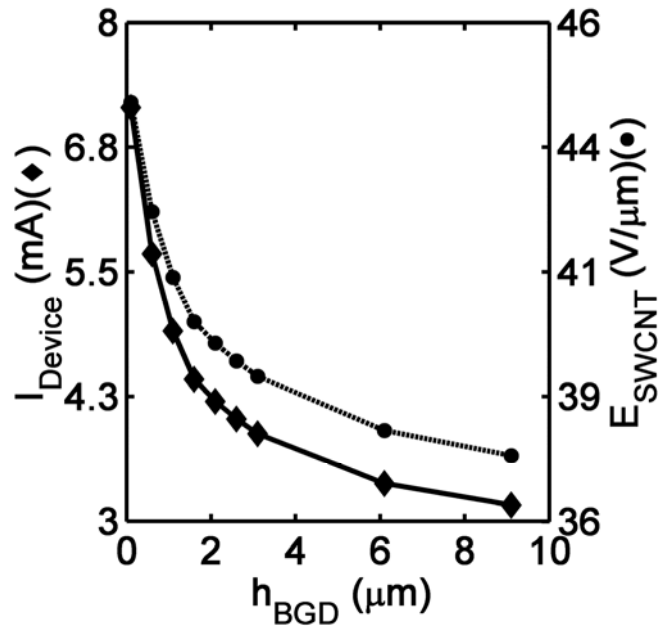


Figure 5. Variation of the maximum integrated current  $I_{optimized}$  and gate metal cathode line separation  $w_{max}$  with the gate bias  $\Phi_{gate}$ . Relevant parameters used:  $\Phi_{Anode} = 200$  V,  $h_{BGD} = 3.1$   $\mu\text{m}$ ,  $h_{gap} = 20$   $\mu\text{m}$ ,  $\gamma_{SWCNT} = 500$ ,  $\epsilon_{BGD} = 4$ .

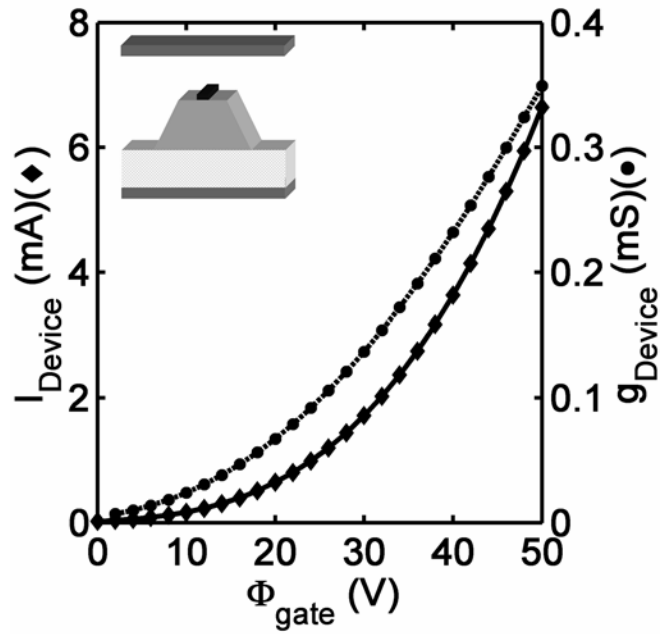


(a)

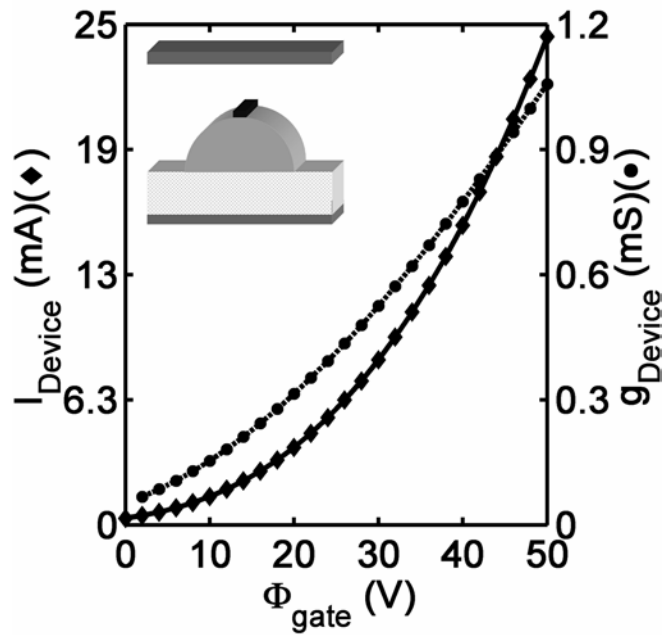


(b)

Figure 6. Variation of the integrated current  $I_{Device}$  and maximum electrostatic field at the EMS surface  $E_{SWCNT}$  with the back gate dielectric structure and material parameters; a) dielectric permittivity  $\epsilon_{BGD}$ , b) thickness  $h_{BGD}$ . Relevant parameters used:  $\Phi_{gate} = 30V$ ,  $\Phi_{Anode} = 200V$ , a)  $h_{BGD} = 3.1 \mu m$ ,  $h_{gap} = 20 \mu m$ ,  $\gamma_{SWCNT} = 500$ , b)  $\epsilon_{BGD} = 4$ ,  $w_{wire} = 6.4 \mu m$ .



(a)



(b)

Figure 7. Variation of the integrated current  $I_{Device}$  and transconductance  $g_{gate}$  with the cathode substrate shape and the gate bias  $\Phi_{gate}$ ; a) a  $\frac{1}{2}$  cylinder of  $r_{wire} = 0.47\mu\text{m}$ , b) a trapezoidal line of  $2r_{wire}=0.94\mu\text{m}$  and  $h_{wire}=0.3\mu\text{m}$ . Relevant parameters used:  $\Phi_{Anode} = 200$  V,  $h_{BGD} = 3.1\mu\text{m}$ ,  $h_{gap} = 20\mu\text{m}$ ,  $\gamma_{SWCNT} = 500$ ,  $\epsilon_{BGD} = 4$ ,  $w_{wire} = 6.4\mu\text{m}$ .

# **Chapter 5. Cold Field Electron Emission from 0D, 1D And 2D Electron Gases**

by

D. L. Jaeger and J. J. Hren

Department of Materials Science and Engineering, North Carolina State University, Raleigh,  
NC 27695-7907

V. V. Zhirnov

Department of Materials Science and Engineering, North Carolina State University, Raleigh,  
NC 27695-7907 and

Semiconductor Research Corporation, Research Triangle Park, North Carolina 27709-2053

Submitted to

Journal of Applied Physics

### 5.1. Abstract

Theoretical analysis is presented for the coherent emission of tunneling electrons from continuous and quantized 1D, 2D and 3D surface electron gases. From this analysis general equations describing the coherent tunneling emission process were developed and applied to the case of a general triangular tunneling barrier. It was demonstrated that the dimensionality of the electron gas has relatively little effect on the emission process compared to the degree of quantization of the electron gas. The emission behavior was also found to vary from normal to saturation limited Fowler-Nordheim tunneling emission, due to the width and relative position of the conduction band with respect to the top of the tunneling barrier.

### 5.2. Introduction

Low dimensional electro-emissive materials, such as films, nanoflakes, nanotubes and nanoparticles, demonstrate a range of interesting properties that enable the design of simple and efficient to fabricate vacuum microelectronic devices<sup>1-3</sup>. Previous work with low dimensional electro-emissive materials indicated that the materials composition, spatial orientation and size can effect the electron emission process, requiring modifications to the tunneling electron supply and potential barrier of the Fowler-Nordheim analysis of such materials<sup>4-7</sup>. A current saturation effect at high applied fields has been observed in some electro-emissive materials used as field emission cathodes, where this behavior has been attributed to mechanisms such as adsorbates<sup>8</sup>, heat induced cathode band structure changes<sup>9</sup>, and space charge effects that limit the supply of electrons available for tunneling<sup>10</sup>.

In this article a theoretical analysis is presented analyzing the effects of dimensionality, quantization and energy band structure on cold field emission. A current limiting carrier saturation mechanism occurring during coherent field emission that is dependent on the material band structure is examined.

### 5.3. Tunneling Equations

The current density of electrons emitted from a material is analyzed assuming a general triangular potential barrier subject to an applied electric field,  $F$ , across which electrons coherently tunnel through quantum mechanically at energies below the top of the barrier,  $E_T$ . The initial energy state of the incident electron to the left of the tunnel barrier is significantly higher than the final energy state to the right of the barrier. The morphology of the surface or interface across which tunneling occurs is assumed to approximate a plane surface at the scale of the period of the electron wavefunction. Further all quantum mechanical electron emission processes are assumed to occur normal to the surface or interface at which emission occurs. Finally the mean free path of electrons in the region of interest is assumed long enough at some temperature that ballistic carrier transport dominates and electron emission is not transport limited<sup>11</sup>.

Assuming electron emission occurs under the above conditions the field emission process can be classified according to the dimensionality and quantization of the surface electron gas, as shown in Figure 1. These conditions are determined by the relative confinement experienced by the electrons along the x, y and z directions, which is determined by the electron phase coherence length in that material<sup>12</sup>. From Figure 1 some general trends are observed, along the top row the surface electron gas is not quantized along

the direction of tunneling and behaves as a quasi-bulk band. Along the bottom row the surface electron gas is constrained along the z-direction and therefore the energy bands are quantized. The degree that the surface electron gas is constrained in the transverse directions,  $t_x$  and  $t_y$ , determines whether emission originates from a 0D, 1D, or 2D electron gas. Constraining the electron gas in the direction normal to the emission surface,  $n_z$ , introduces mini-bands in the 1D and 2D electron gas and fully quantizes the 0D electron gas into a discrete set of states.

For the general coherent tunneling problem the initial energy of the electron may be written as  $E = E_z + E_t$ , where  $E_z$  is the energy normal to the interface and  $E_t$  is the energy transverse to the interface. Assuming that the bands are parabolic and electron motion is coherent/unconstrained in the direction normal to the interface, such that the bands are continuous in the z-direction, the total energy relative to the band edge is  $E_{b,k} = E_k + E_b$ , where  $E_k$  is the energy parallel to the interface and  $E_b$  is the band edge energy. The density of states of the general system can then be found from

$$g(E_t, E_z) = \sum_{\alpha_s, \eta_v, k} \delta(E - E_{b,k}) \quad (1)$$

where  $\alpha_s$  is the spin degeneracy and  $\eta_v$  is the valley degeneracy. Transforming the sum into an integral the density of states per unit area for electrons tunneling from 1D, 2D and 3D structures is

$$g_{0D}(E_t, E_z) = \frac{\alpha_s \eta_v}{2} \Theta(E_z - E_b) \delta(E_t - E_b) \quad (2)$$

$$g_{1D}(E_t, E_z) = \frac{\alpha_s \eta_v}{4\pi} \sqrt{\frac{2m_0 m_r}{\hbar^2}} \frac{\Theta(E_z - E_b) \Theta(E_t - E_b)}{\sqrt{E_t - E_b}} \quad (3)$$

$$g_{2D}(E_t, E_z) = \frac{\alpha_s \eta_v}{4\pi} \left( \frac{2m_0 m_r}{\hbar^2} \right) \Theta(E_z - E_b) \Theta(E_t - E_b) \quad (4)$$

where  $m_r$  is the effective mass of the tunneling electron. The density of electrons in equilibrium available for tunneling is

$$n(E_z) = \int_{-\infty}^{\infty} dE_t g(E_t, E_z) f_0(E_t, E_z) \quad (5)$$

where  $T_l$  is the lattice temperature and  $f_0(E_t, E_z)$  is the equilibrium Fermi distribution function. The density of electrons in equilibrium available for tunneling from 0D, 1D and 2D electron gases in the low temperature limit, where  $f_0(E_t, E_z) = \Theta(E_f - E_z) \Theta(E_f - E_t)$ , are

$$n_{0l} = n_{00} \Theta(E_z - E_b) \Theta(E_f - E_z) \quad (6)$$

$$n_{1l} = 2n_{10} \sqrt{E_f - E_z} \Theta(E_z - E_b) \quad (7)$$

$$n_{2l} = n_{20} (E_f - E_z) \Theta(E_z - E_b) \quad (8)$$

where  $n_{00} = \frac{\alpha_s \eta_v}{2}$ ,  $n_{10} = \frac{\alpha_s \eta_v}{4\pi} \sqrt{\frac{2m_0 m_r}{\hbar^2}}$ , and  $n_{20} = \frac{\alpha_s \eta_v}{4\pi} \left( \frac{2m_0 m_r}{\hbar^2} \right)$ .

The WKB approximation of the triangular barrier quantum tunneling probability,  $T_z$ , can be written as

$$T_z(E_z, F) \simeq T_{WKB}(E_z, F) = \begin{cases} \exp\left(-\frac{A|E_z|^{3/2}}{\gamma F}\right) & E_z < 0 \\ 1 & E_z \geq 0 \end{cases} \quad (9)$$

where  $A = \frac{4\sqrt{2m_0 m_r}}{3\hbar e}$  and  $\gamma$  is the local electrostatic field enhancement factor at the

interface/surface. If the majority of electrons available which tunnel have energies near an

energy  $E_p$  below the top of the barrier the argument to the exponent can be approximated by a Taylor series expansion about the energy  $E_p$  such that

$$T_p(E_z, F) = \begin{cases} \exp(-a_p) \exp(b_p(E_z - E_p)) & E_z < 0 \\ 1 & E_z \geq 0 \end{cases} \quad (10)$$

where  $a_p = \frac{A(-E_p)^{3/2}}{\gamma F}$  and  $b_p = \frac{3}{2(-E_p)} a_p$ .

The Normal Energy Distribution,  $j'$ , of electrons that tunnel through the barrier is given by the product of the transmission coefficient and the electron density at the interface

$$j'(E_z, F) = n(E_z) T_z(E_z, F) \quad (11)$$

and the tunnel electron current density is

$$J = \frac{e}{h} \int_{-\infty}^{\infty} j'(E_z, F) dE_z. \quad (12)$$

The electron energy where the normal energy distribution is a maximum is found by minimizing the derivative of the normal energy distribution with respect to the electron energy,  $\frac{dj'}{dE_z}$ . Substituting the barrier transmission probability is given by (10) and the

electron density functions are given by (6-8) into (11) then  $E_{p,dD}^{j'.WKB}$  represents the ideal energy about which to perform a Taylor expansion of the WKB tunnel probability (9) for a  $d$

dimensional electron gas, where in terms  $\kappa = -\frac{2}{3} \left( \frac{A(-E_f)^{3/2}}{F_{local}} \right)^2$

$$E_{p,0D}^{j'.WKB} = E_f \quad (13)$$

$$E_{p,1D}^{j,WKB} = \frac{E_f}{6} \left( -\frac{2}{\kappa} \right)^{1/3} \frac{\left( (-4\kappa)^{1/3} + (1 + \sqrt{1-4\kappa})^{2/3} \right)^2}{(1 + \sqrt{1-4\kappa})^{2/3}} \quad (14)$$

$$E_{p,2D}^{j,WKB} = \frac{E_f}{3} \Re \left[ \left( -\frac{1}{\kappa} \right)^{1/3} \frac{\left( (-\kappa)^{1/3} + (1 + \sqrt{1+\kappa})^{2/3} \right)^2}{(1 + \sqrt{1+\kappa})^{2/3}} \right]. \quad (15)$$

Assuming that emission occurs in the low temperature limit,  $T_l = 0K$ , and that  $E_f$  is less than the top of the barrier then the current density is

$$J_{dD} = \frac{e}{h} \int_{E_b}^{E_f} n_{dD}(E_z) T_p(E_z, F) dE_z. \quad (16)$$

where in terms of the emission area  $\alpha$  the emission current may be expressed as  $I_{dD} = \alpha^{d/2} J_{dD}$ . The resulting general current density equations for cold field emission from  $n=0,1$ , and 2 D surface electron gases are

$$J_{0D} = J_{0D, FN} \exp(-\xi) \{1 - \exp(-\nu)\} \quad (17)$$

$$J_{1D} = J_{1D, FN} \exp(-\xi) \left( \operatorname{erf}(\sqrt{\nu}) - \frac{2}{\sqrt{\pi}} \sqrt{\nu} \exp(-\nu) \right) \quad (18)$$

$$J_{2D} = J_{2D, FN} \exp(-\xi) (1 - (1 + \nu) \exp(-\nu)) \quad (19)$$

where  $\xi = b_p (E_p - E_f)$ ,  $\nu = b_p (E_f - E_b)$  and  $\operatorname{erf}(x)$  is the error function. As  $E_b \rightarrow -\infty$  and assuming most electrons are emitted near the Fermi energy,  $E_p = E_f$ , the above equations reduce to the classical Fowler Nordheim expressions

$$J_{0D, FN} = \frac{e}{h} n_{00} \frac{\exp(-a_p)}{b_p} \quad (20)$$

$$J_{1D, FN} = \frac{e}{h} n_{10} \frac{\sqrt{\pi} \exp(-a_p)}{b_p^{3/2}} \quad (21)$$

$$J_{2D, FN} = \frac{e}{h} n_{20} \frac{\exp(-a_p)}{b_p^2}. \quad (22)$$

Applying classical FN data analysis to the previous equations and assuming that  $E_b \rightarrow -\infty$  and  $E_p = E_f$  results in the general equation

$$\ln\left(\frac{J_{dD,0}}{F^2}\right) = -A_d \frac{1}{F} + B_d - C_d \ln(F) \quad (23)$$

where the fit parameters are given in Table I. The coefficients to the general equation are found by applying a least-square linear in the parameters fit of data to the model with  $|E_p|$  and  $\gamma$  extracted from these parameters, which are given in Table I. The new parameter  $C_d$  contains information on dimensionality of the surface electron gas and indicates the degree of nonlinearity in the FN plots due to electron confinement in directions parallel to the tunneling interface.

Quantization of the allowed electron levels, as shown schematically in the bottom row of Figure 1, result in the formation of sub-bands and discrete energy levels for 0D, 1D, and 2D electron gases located at interfaces. As in the case of continuous bands quantization effects parallel to the emission interface are incorporated in the equilibrium electron densities,  $n_{dD}(E_z)$ . In 1D and 2D surface electron gases along at least one direction parallel to the interface electron motion is unrestricted and therefore sub-band structures with quasi band edges develop. The quasi band edges are  $E_N = E_b + \Delta E_{dD}$ , where  $\Delta E_{dD}$  is the change

in energy due to quantization. In the low temperature limit the calculation of current density is restricted to  $E_N \geq E_z \geq E_f$ , such that  $\xi = \xi_N$  and  $\nu = \nu_0 - b_p \Delta E_{dD,N}$  are substituted into the current density relations. The quantized 0D electron gases develop discrete levels in the z-direction due to the restricted motion of electrons in all directions and lack of sufficient thermal energy to excite electrons from one level to another, such that  $\Delta E_{qD} > k_B T_L$  and the current density is

$$J_{0D,N} = \frac{e}{h} n_{00} T_z(E_N) \left( 1 - \left( 1 - \exp\left(-\frac{E_N - E_f}{k_B T_L}\right) \right) \Theta(E_N - E_f) \right). \quad (24)$$

The resulting total current density is the sum of the sub-band and discrete level current densities

$$J_{dD} = \sum_N J_{dD,N}. \quad (25)$$

#### 5.4. Results and Discussion

Emission was assumed to occur from a clean, high aspect ratio surface,  $\gamma = 20$ , at  $T_l = 0K$ , where emission is not limited by electron transport from the bulk to the surface and surface space charge effects, such that cold field emission is assumed to be the only emission process available. The substrate material is assumed to be metallic in nature with  $m_r = 1$  and  $\eta_v = 1$ . The current density was calculated either analytically or numerically, where the transmission coefficient was calculated using either the WKB approximation (27), with  $E_p = E_f$ , or the Quantum Transmitting Boundary Method (QTBM)<sup>13</sup>.

Calculations of the integrated current density for low dimensional structures as seen in Figure 1 were performed. The average error between the analytical and WKB numerical results was within 3 percent and between the WKB and QTBM results was approximately 50

percent. For typical metal emitter parameters the numerical and analytical current density results displayed pure FN behavior. For a material with  $E_f = -4.6eV$ ,  $E_p = -10.6eV$ ,  $\gamma = 20$  and continuous bands the field emission approximates classical FN behavior, as shown in Figure 3a region I, where electron transmission through the barrier controls emission. The influence of dimensionality on the current density does not produce noticeable structural artifacts, such that comparison of such data would not lead to a definitive conclusion on the dimensionality of the electron gas.

Linearizing the numeric data of Fig. 3a into a FN plot, (37) and Table I, and a best fit to that fit to that data is shown in Fig. 3b. The negative slopes indicate that classical FN behavior is the dominant emission mechanism in the range of fields plotted. The derived  $\gamma$  were calculated by substituting  $E_p = -0.4eV$  into the value for  $\gamma$  given in Table I, where there is good agreement between the actual and derived values of  $\gamma$ . The nonlinearity of the 0D and 1D plots in comparison to the 2D plot is indicative of the dimensionality of the electron gas, where the parameters  $C_d$  of the fitted data agree with those given in Table I, indicating that dimensionality of the electron gas can be extracted from analysis of such linearized data.

As the band minimum was brought closer to the Fermi energy and the Fermi energy brought nearer the top of the potential barrier the current density increasingly no longer displayed pure FN behavior. For a material with  $E_f = -0.4eV$ ,  $E_p = -0.8eV$ ,  $\gamma = 20$  and continuous bands Figure 4a shows that for low applied fields the emission approximates classical FN behavior, region I, where emission is controlled by electron transmission through the barrier. At higher fields a current limiting mechanism causes the field emitted current density to become saturated, region II, where emission is controlled by the electron

supply available for tunneling, as shown in the percentage of electrons emitted as a function of the applied field which saturates to approximately 60% of all available electrons. In comparison the maximum percentage of electrons emitted for the same applied fields for the material considered in Fig. 3 was 1% of all available electrons.

Linearizing the numeric data of Fig. 4a into a FN plot, (37) and Table I, and a best fit to that fit to that data is shown in Fig. 4b. The positive slopes is demonstrative that classical FN behavior is not the dominant emission mechanism in the range of fields plotted. The derived  $\gamma$  were calculated by substituting  $E_p = -0.4eV$  into the value for  $\gamma$  given in Table I. Poor agreement between the actual and derived values of  $\gamma$  and the parameters  $C_d$  of the fitted data with those of Table I was found. This was attributed to the derivation of (27) from the classical FN relations (31-33) which do not account for a limited electron supply.

The onset of the saturation component is observable in Figure 5, where the applied field where the maximum transconductance occurs is approximately the point current saturation occurs. Dimensionality does not have a significant effect on the position of the maximum transconductance and the for a 1nm or 1X1nm area the 0D structure appears to display the largest transconductance by a factor of approximately 2. For applied fields before this spike in the transconductance the current density translates from pure FN behavior to current limited FN behavior.

This can impact the use of FN analysis to extract meaningful energy band and field enhancement values as seen in Figure 6, where the current saturation component can strongly effect the derived FN values and complicate data analysis. It is possible to remove this artifact by further limiting the applied fields over which FN analysis is performed.

The approximate contribution of the saturation component to the emission process is shown in Figure 7 as the saturation transconductance ratio which for no transconductance spike is 1 and for the presence and relative strength of the transconductance spike less than 1. The band minimum threshold energy at which the transconductance spike first appears is greatest for 0D structures and the least for the 2D structures. The current limiting mechanism responsible for the saturation effect is shown in Figure 7 as the percentage of the electrons being emitted are a significant fraction of the total electrons in the band, such that at  $E_b = -0.6\text{eV}$  approximately 90% of the available electrons are emitted and relatively few electrons remain to be emitted.

The saturation component is nearly nonexistent for fairly deep Fermi energies as seen in the variation of the threshold field in Figure 8 with respect to the Fermi energy. In this region the maximum current at the threshold energy is roughly linear, this is explained by the linear variation in the threshold energy and nearly linear variation of the transmission coefficient in this region. As  $E_f$  decreases the dimensionality of the material effects the relative rate at which  $E_t$  decreases, as seen in the rapid decrease in 0D result, which is due to higher percentage of emitted electrons compared to the 1D and 2D results as shown in Figure 7.

The threshold energy for 80% agreement between the pure and general FN equations,  $E_s(0.8)$ , in Figure 8 when compared to  $E_f$  indicates that for deep Fermi levels the percentage agreement between the pure and general FN analysis is less than 80%, however for shallow Fermi levels the agreement between the two is approximately 80% for the 2D case, 93% for the 1D case and 99% for the 0D case. Therefore the relative agreement of the classical FN analysis with the general FN analysis, the appearance of the transconductance

spike and the strength of the saturation effect are determined by the location of the Fermi level in relation to the top of the barrier and depth of the band.

### 5.5. Conclusions

A model based on the classical FN formalism was proposed to describe cold field electron emission from 0D, 1D and 2D surface electron gases. The dimensionality of the emissive structure introduced nonlinear terms into the FN analysis, however no structural features in the current densities were observed that could be associated with dimensionality. The dominant emission mechanism was observed to be either transmission or electron supply limited emission. The electron supply limited field emission regime caused current saturation at high applied fields, where current is limited by the width and position of the surface electron supply in relation to the top of the potential barrier.

### 5.6. References

- <sup>1</sup> W. B. Choi, J. J. Cuomo, V. V. Zhirnov, A. F. Myers, and J. J. Hren, *Appl. Phys. Lett.* **68**, 720 (1996).
- <sup>2</sup> A.P. Burden, *Intl. Matls. Rev.*, **46**, 213 (2001).
- <sup>3</sup> V.P. Mammana, D. Jaeger, O. Shenderova, G.E. McGuire, *J. Vac. Sci. Technol. A*, **22**, 1455 (2004).
- <sup>4</sup> V.G. Litovchenko, A.A. Evtukh, Y.M. Litvin, N.M. Goncharuk, H. Hartnagel, O. Yilmazoglu, D. Pavlidis, *Appl. Surf. Sci.*, **215**, 160 (2003).
- <sup>5</sup> V. Filip, D. Nicolaescu, H. Wong, M. Nagao, P.L. Chu, *J. Vac. Sci. Technol. B*, **23**, 657 (2005).

- 
- <sup>6</sup> R.G. Forbes, *Solid State Electronics*, **45**, 779 (2001).
- <sup>7</sup> P.H. Cutler, J. He, N.M. Miskovsky, T.E. Sullivan, B. Weiss, *J. Vac. Sci. Technol. B*, **11**, 387 (1993).
- <sup>8</sup> K.A. Dean, B.R. Chalamala, *Appl. Phys. Lett.*, **76**, 375 (2000).
- <sup>9</sup> S.K. Patra, G.M. Rao, *J. Appl. Phys.*, **100**, 024319 (2006).
- <sup>10</sup> E. I. Givargizov, V. V. Zhirnov, A. V. Kuznetsov, and P. S. Plekhanov, *J. Vac. Sci. Technol. B.*, **14**, 2030 (1996).
- <sup>11</sup> G. Furse, *Field Emission in Vacuum Microelectronics*, (Kluwer Academic, New York, 2005).
- <sup>12</sup> D.K. Ferry and S.M. Goodnick, *Transport in Nanostructures*, (Cambridge University press, Cambridge, UK, 1997).
- <sup>13</sup> C.S. Lent, D.J. Kirkner, *J. Appl. Phys.*, **67**, 6353 (1990).

Table I. Fit parameters for the least squares analysis of the general FN plot analysis and extracted material parameters.

$d D$	$A_d$	$B_d$	$C_d$	$ E_{p,d} $	$\gamma_d$
0	$\frac{A E_{p,0} ^{3/2}}{\gamma_0}$	$\ln\left(\frac{en_{00}}{h} \frac{2 E_{p,0} }{3A_0}\right)$	1	$\frac{3}{2}A_0\left(\frac{h\exp(B_0)}{en_{00}}\right)$	$\frac{A}{A_0} E_{p,0} ^{\frac{3}{2}}$
1	$\frac{A E_{p,1} ^{3/2}}{\gamma_1}$	$\ln\left(\frac{e\sqrt{\pi}n_{10}}{h}\left(\frac{2 E_{p,1} }{3A_1}\right)^{3/2}\right)$	$\frac{1}{2}$	$\frac{3}{2}A_1\left(\frac{h\exp(B_1)}{\sqrt{\pi}en_{10}}\right)^{\frac{2}{3}}$	$\frac{A}{A_1} E_{p,1} ^{\frac{3}{2}}$
2	$\frac{A E_{p,2} ^{3/2}}{\gamma_2}$	$\ln\left(\frac{en_{20}}{h}\left(\frac{2 E_{p,2} }{3A_2}\right)^2\right)$	0	$\frac{3}{2}A_2\left(\frac{h\exp(B_2)}{en_{20}}\right)^{\frac{1}{2}}$	$\frac{A}{A_2} E_{p,2} ^{\frac{3}{2}}$

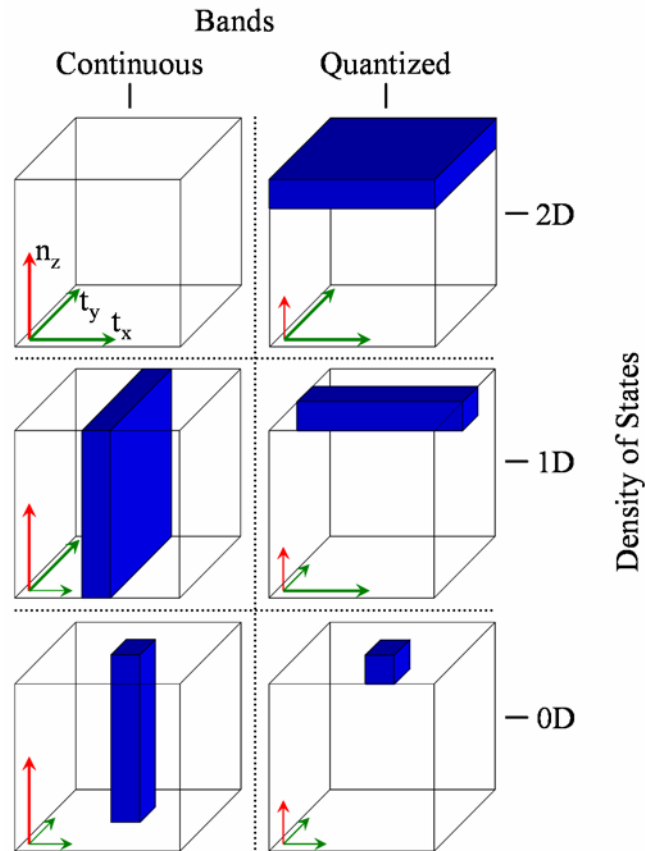


Figure 1. Schematic of general low dimensional electron emitting structures, in blue, and the surrounding bulk material that constitute the active region of a field emitter cathode. Electron emission occurs in the  $z$  axis direction and the relative length of the axis vectors indicates the degree of electron confinement in those particular directions. The tunneling electron is emitted from a surface electron gas whose dimensionality varies horizontally and degree of quantization varies vertically.

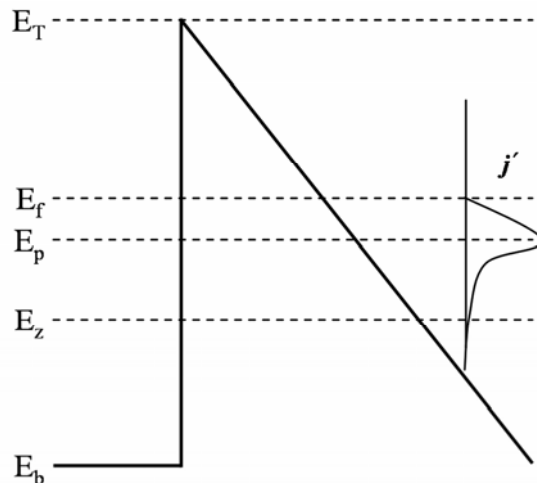


Figure 2. General triangular potential seen from an electron traversing from the left at energy  $E_z$ , where  $E_b$  is the band minimum,  $E_f$  is the Fermi energy,  $E_p$  is ideally the energy at which a maximum amount of electrons can quantum mechanically tunnel through the potential barrier, and  $E_T$  is the top of the potential barrier, typically the local vacuum level.

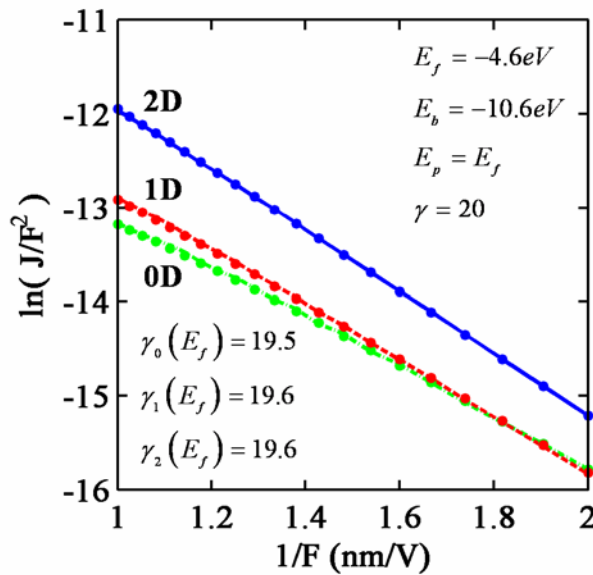
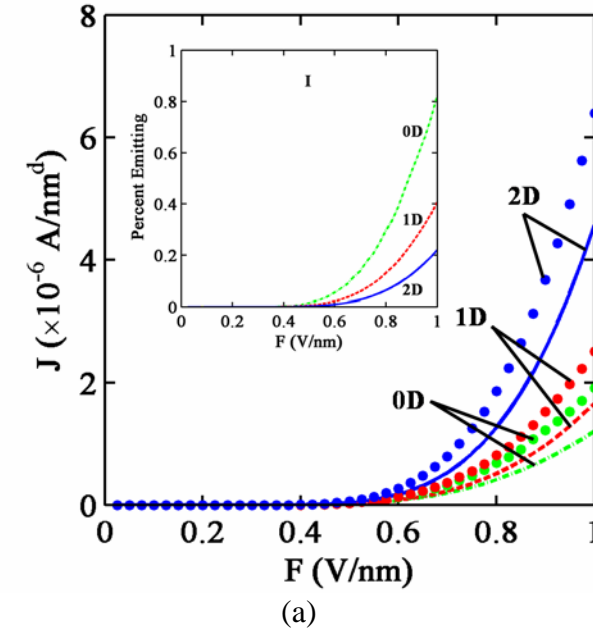
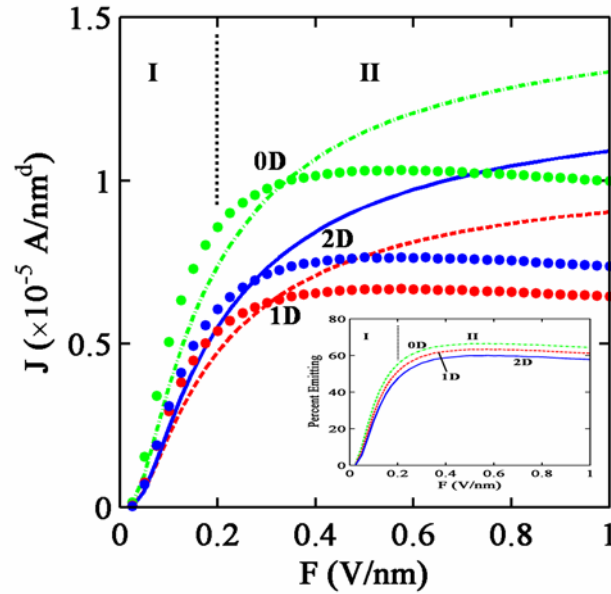
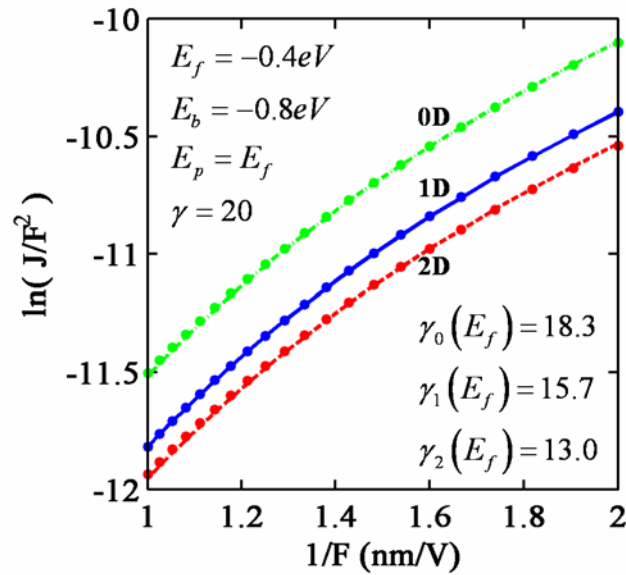


Figure 3. Analytical FN and numerical QTBM calculations of (a) current densities and (b) Linearized Fowler-Nordheim plots, denoted by lines and markers respectively, for the case of  $d$ -dimensional structures with continuous bands and parameters  $E_b = -10.6 eV$ ,  $E_f = -4.6 eV$ , and  $E_p = E_f$ , displaying classical Fowler-Nordheim tunneling where electron emission is limited by quantum barrier tunneling.



(a)



(b)

Figure 4. Analytical FN and numerical QTBM calculations of (a) current densities and (b) Linearized Fowler-Nordheim plots, denoted by lines and markers respectively, for the case of  $d$ -dimensional structures with continuous bands and parameters  $E_b = -0.8eV$ ,  $E_f = -0.4eV$ , and  $E_p = E_f$ , displaying saturation behavior where electron emission is limited by quantum barrier tunneling in region I and by the electron supply in region II.

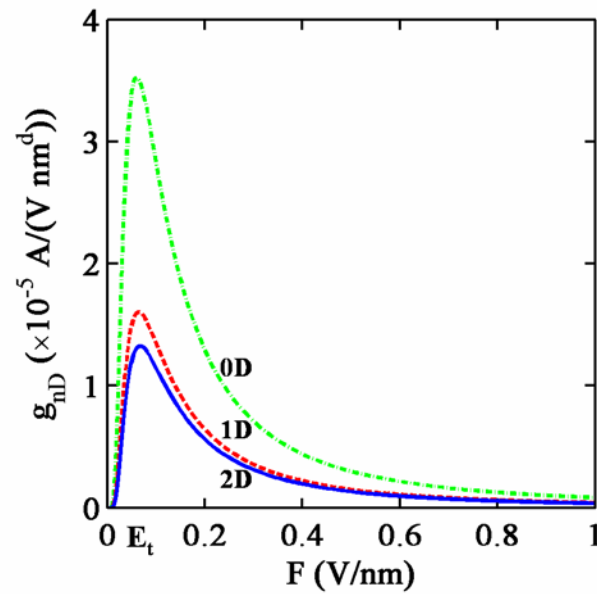


Figure 5. Analytical FN calculations of transconductance for the case of low dimensional structures with continuous bands and parameters  $E_b = -0.6eV$ ,  $E_f = -0.4eV$ , and  $E_p = E_f$ , where the approximate onset of saturation behavior is observed near the maximum transconductance.

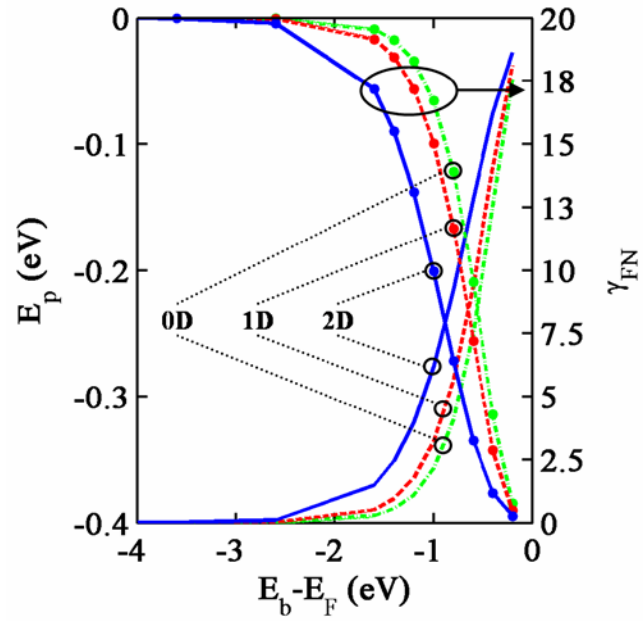


Figure 6. From WKB numerical current densities the calculated FN parameters  $E_p$  and  $\gamma_{FN}$ , denoted by lines and lines + markers respectively, are shown for low dimensional structures with continuous bands and parameters  $E_f = -0.4eV$ ,  $E_p = E_f$  and  $\gamma_{FN} = 20$ . The applied fields were limited up to the maximum transconductance.

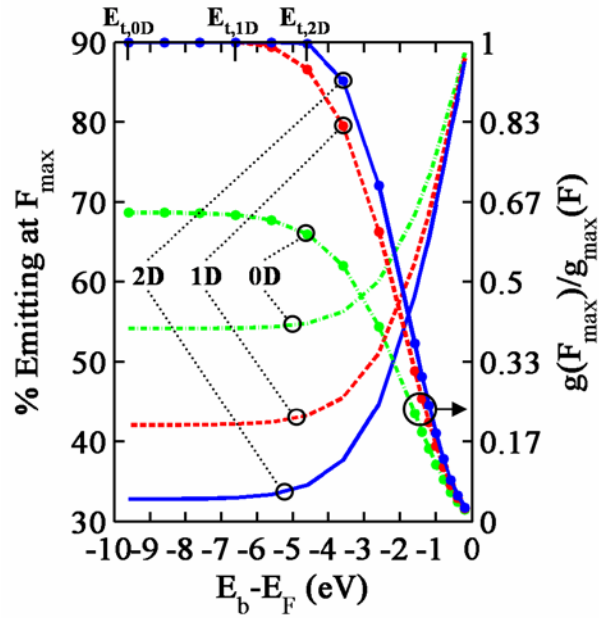


Figure 7. The percent of electrons emitted and the saturation transconductance ratio,  $g(F_{\max})/g_{\max}(F)$ , at the maximum transconductance, denoted by lines and lines + markers respectively, for low dimensional structures with continuous bands and parameters  $E_f = -0.4\text{eV}$  and  $E_p = E_f$ . The threshold energies at which the saturation component has an effect on the emission process are indicated by  $E_{t,mD}$  at the top of the graph.

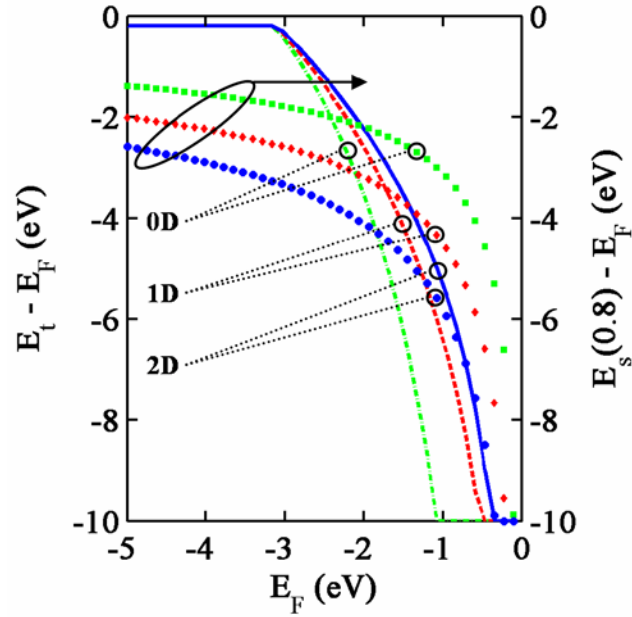


Figure 8. From WKB numerical calculations the variation of the saturation threshold energies,  $E_t$ , and the energy at which the saturation FN equations agree within 80% to the pure FN equations,  $E_s(0.8)$ , denoted by lines and markers respectively, are shown for low dimensional structures with continuous bands and parameters  $E_p = E_f$  and  $\gamma_{FN} = 20$ .

## Chapter 6. Summary

### 6.1. Geometric electrostatic field effects on field emission

Geometric and material parameters affecting field electron emission were analyzed for device structures incorporating low dimensional cathodes that permit simplified processing. Electrostatic shielding effects due to cathode density was demonstrated for diode type cathodes and multistage structures to strongly affect the emission process with the maximum current for an array being strongly peaked about an optimized cathode spacing. Cathode surface inhomogeneities were demonstrated to have a strong local effect on the surface fields, where this local field enhancement results in either reliability issues or a means to deterministically enhance emission.

The triple junction at the metal-dielectric-vacuum interface for semi-embedded and conformal dielectric particles was affected by a combination of geometric and material effects. A shift in the maximum field strength from the metal-dielectric to dielectric interface was observed for the conformal and semi-embedded particles as a function of cathode geometry, size and material. This size and geometric dependence is a concern since for many deposition techniques a size range of particles or deposit is assumed, therefore the emission efficiency of a cathode may be affected.

Further work on the effects of particle trajectories from the emission sites is needed for a proper understanding of the electron optics of a device and the triple junction effect on tunneling. A study of the image potential of the particle systems studied as a function of the particle size and geometry could offer insight on the size dependence of the image potential in relation to the classical image potential model.

## 6.2. Dimensionality effects on field emission

Forms of the vacuum field emission equations analogous to the classical Fowler-Nordheim equations were derived with additional conditions set for the cathode band structure. The dimensional differences of 0D, 1D and 2D surface electron gases were observed in the linearized FN analysis as non-linearities compared to results for a 2D electron gas. A transition from barrier controlled emission, classical FN emission, and electron supply controlled emission was observed as a function of the band width and location in relation to the top of the potential barrier. Electron supply controlled emission can result in strong current saturation, which is attractive for devices as a simple and efficient method to increase reliability and controllability of diode type field emission cathode arrays.

## 6.3. Suggested Future Work

Further work on the effects of particle trajectories from the emission sites is needed for a proper understanding of the electron optics of a device and the triple junction effect on tunneling. A study of the image potential of the particle systems studied as a function of the particle size and geometry could offer insight on the size dependence of the image potential in relation to the classical image potential model.

The inclusion of discrete dopant effects would prove useful in understanding the validity of the present work to doped dielectric nanostructures, such as nanodiamond particles<sup>1</sup>. The size of the structures considered in this research is such that the 1D approximation used to develop the conventional field emission may be inadequate requiring the use of a 3 dimensional tunneling transmission coefficient calculation<sup>2</sup>. Finally, effects

not considered in this research, such as thermionic effects, classical image potential effects and multiple potential barriers, should be considered for inclusion as modifications to the derived low dimensional field emission equations.

#### 6.4. References

- <sup>1</sup> A.V. Kvit, V.V. Zhirnov, T. Tyler, J.J. Hren, *Composites B*, **35**, 163 (2004).
- <sup>2</sup> P.A. Sundqvist, Q.X. Zhao, M. Willander, *Phys. Rev. B*, **72**, 165103 (2005).